# Dynamically Orthogonal Numerical Schemes for Efficient Stochastic Advection and Lagrangian Transport*

Florian Feppon[†]
Pierre F. J. Lermusiaux[†]

**Abstract.** Quantifying the uncertainty of Lagrangian motion can be performed by solving a large number of ordinary differential equations with random velocities or, equivalently, a stochastic transport partial differential equation (PDE) for the ensemble of flow-maps. The dynamically orthogonal (DO) decomposition is applied as an efficient dynamical model order reduction to solve for such stochastic advection and Lagrangian transport. Its interpretation as the method that applies the truncated SVD instantaneously on the matrix discretization of the original stochastic PDE is used to obtain new numerical schemes. Fully linear, explicit central advection schemes stabilized with numerical filters are selected to ensure efficiency, accuracy, stability, and direct consistency between the original deterministic and stochastic DO advections and flow-maps. Various strategies are presented for selecting a time-stepping that accounts for the curvature of the fixed-rank manifold and the error related to closely singular coefficient matrices. Efficient schemes are developed to dynamically evolve the rank of the reduced solution and to ensure the orthogonality of the basis matrix while preserving its smooth evolution over time. Finally, the new schemes are applied to quantify the uncertain Lagrangian motions of a 2D double-gyre flow with random frequency and of a stochastic flow past a cylinder.

## Contents

**1. Introduction.** Advection plays a major role in a wide variety of physical processes and engineering applications of fluid mechanics [26, 3], neutronic transport, chemical transports, atmospheric sciences [62], and ocean sciences [20, 53]. At its most fundamental level, the pure advection process is commonly understood through the transport partial differential equation (PDE),

$$(1) \qquad \begin{cases} (\partial_t + \boldsymbol{v}(t, \boldsymbol{x}) \cdot \nabla)\boldsymbol{\psi} = 0, \\ \qquad \boldsymbol{\psi}(0, \boldsymbol{x}) = \boldsymbol{\psi}_0(\boldsymbol{x}), \end{cases}$$

which models the material transport of a passive (scalar or vectorial) tracer field $\boldsymbol{\psi}$ under a velocity field $\boldsymbol{v}$, having its values initially distributed as $\boldsymbol{\psi}_0$ over a physical domain $\Omega \subset \mathbb{R}^d$ of positions $\boldsymbol{x}$. Another description of transport considers a parcel of material initially located at the location $\boldsymbol{x}_0$ and transported to the position $\boldsymbol{\phi}_0^t(\boldsymbol{x}_0) = \boldsymbol{x}(t)$ with instantaneous velocity $\boldsymbol{v}(t, \boldsymbol{x}(t))$. In this Lagrangian description, $\boldsymbol{x}(t)$ is the solution of the ordinary differential equation (ODE)

$$(2) \qquad \begin{cases} \dot{\boldsymbol{x}} = \boldsymbol{v}(t, \boldsymbol{x}(t)), \\ \boldsymbol{x}(0) = \boldsymbol{x}_0, \end{cases}$$

and $\boldsymbol{\phi}_0^t$, i.e., the function mapping the initial positions $\boldsymbol{x}_0$ to $\boldsymbol{\phi}_0^t(\boldsymbol{x}_0) = \boldsymbol{x}(t)$ at time $t$, is the *flow-map* of the ODE (2). Under sufficient regularity conditions on the velocity field $\boldsymbol{v}$ [9, 2], the solution $\boldsymbol{\psi}$ of the advection equation (1) relates to equation (2) as being obtained by "carrying $\boldsymbol{\psi}_0$ values along the particles' paths":

$$(3) \qquad \boldsymbol{\psi}(t, \boldsymbol{x}) = \boldsymbol{\psi}_0((\boldsymbol{\phi}_0^t)^{-1}(\boldsymbol{x})),$$

where $(\boldsymbol{\phi}_0^t)^{-1}$ is the backward or inverse flow-map (Figure 1). In fact, (1) and (2) are equivalent mathematical descriptions of material transport, as setting $\boldsymbol{\psi}_0(\boldsymbol{x}) = \boldsymbol{x}$ in (3) yields $\boldsymbol{\psi}(t, \boldsymbol{x}) = (\boldsymbol{\phi}_0^t)^{-1}(\boldsymbol{x})$. Similarly, solving the transport equation backward in time with the terminal condition $\boldsymbol{\rho}^t(\boldsymbol{x})$,

$$(4) \qquad \begin{cases} (\partial_s + \boldsymbol{v}(s, \boldsymbol{x}) \cdot \nabla)\boldsymbol{\rho} = 0, \\ \qquad \boldsymbol{\rho}(t, \boldsymbol{x}) = \boldsymbol{\rho}^t(\boldsymbol{x}), \end{cases}$$

allows us to retrieve the forward flow-map from the relation $\boldsymbol{\rho}(s, \boldsymbol{x}) = \boldsymbol{\rho}^t(\boldsymbol{\phi}_s^t(\boldsymbol{x}))$ by setting $\boldsymbol{\rho}^t(\boldsymbol{x}) = \boldsymbol{x}$. This shows that the flow-map $\boldsymbol{\phi}_0^t$ can be obtained from a
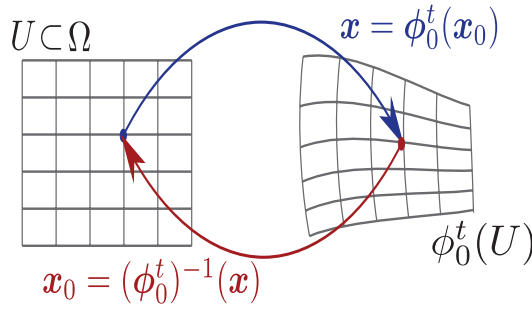
**Fig. 1** *Illustration of the action of the forward and backward flow-map on a subdomain $U \subset \Omega$ of a spatial domain $\Omega \subset \mathbb{R}^d$. $\phi_0^t$ maps initial particle positions $\boldsymbol{x}_0$ to their position at time $t$, and $(\phi_0^t)^{-1}$ is the reciprocal map.*

solution of the transport PDE (1), and vice versa. This property has been thoroughly investigated on the theoretical side to provide a mathematical meaning to the solutions of the ODE (2) for velocity fields $\boldsymbol{v}$ with weak regularity [9, 2, 4], and more recently in numerical computations, as it offers an alternative method to direct particle advection for the evaluation of the flow-map $\phi_0^t$ [44, 45].

   A typical challenge encountered in environmental flow predictions is the need to deal with velocity data that include a certain level of uncertainty, resulting from sparse data acquisitions, noise in direct measurements, or errors in the inferred numerical predictions [41]. Uncertainty is modeled by including randomness in the velocity field [39]: each realization, $\boldsymbol{v}(t, \boldsymbol{x}; \omega)$, corresponds to a particular possible scenario, $\omega$. An issue of great interest in hazard predictions [33] is to quantify how this uncertainty reverberates in the Lagrangian motion [42]. A basic Monte Carlo (MC) approach would then solve either the stochastic ODE

$$(5) \qquad \begin{cases} \dot{\boldsymbol{x}} = \boldsymbol{v}(t, \boldsymbol{x}; \omega), \\ \boldsymbol{x}(0) = \boldsymbol{x}_0, \end{cases}$$

or the stochastic PDE (SPDE)

$$(6) \qquad \begin{cases} \partial_t \boldsymbol{\psi} + \boldsymbol{v}(t, \boldsymbol{x}; \omega) \cdot \nabla \boldsymbol{\psi} = 0, \\ \boldsymbol{\psi}(0, \boldsymbol{x}) = \boldsymbol{x}, \end{cases}$$

for a large number of realizations, $\omega$. While performance of particle as well as MC methods can be optimized through parallelism, such methodologies are computationally demanding for cases requiring high resolution in both the spatial and stochastic domains, i.e., large numbers of particles and realizations. Hence, while they have been useful in a variety of applications [6, 46], particle and MC methods are very expensive for uncertain advection.

   A substantial benefit of the PDE formulation (6) is its compatibility with dynamical model order reduction, which takes direct advantage of the spatial structures in the solution. Classic reduced-order methods aim to evolve low-rank decompositions such as $\boldsymbol{\psi}(t, \boldsymbol{x}; \omega) \simeq \sum_{i=1}^{r_\Psi} \zeta_i(t; \omega) \boldsymbol{u}_i(\boldsymbol{x})$ or $\boldsymbol{\psi}(t, \boldsymbol{x}; \omega) \simeq \sum_{i=1}^{r_\Psi} \zeta_i(\omega) \boldsymbol{u}_i(t, \boldsymbol{x})$, at a cost much smaller than the direct realization methods [75, 19], by independently evolving a small number $r_\Psi$ of spatial modes, $\boldsymbol{u}_i$, or stochastic coefficients, $\zeta_i$. For model order reduction of SPDEs, classic methods such as polynomial chaos

[56, 28, 84, 13], proper orthogonal decomposition (POD) [26, 60], dynamic mode decomposition (DMD) [61, 66, 78, 82, 31], and stochastic Galerkin schemes and adjoint methods [10, 7] assume a priori choices of time-independent modes $\boldsymbol{u}_i(\boldsymbol{x})$ and/or rely on Gaussianity assumptions on the probability distribution of the coefficients $\zeta_i$. For example, the popular data POD [26] and DMD [66] methods suggest extracting time-independent modes $\boldsymbol{u}_i(\boldsymbol{x})$ that respectively best represent the variability (for the POD method) or the approximate linear dynamics (for the DMD method) of a series of snapshots $\boldsymbol{u}(t_k, \boldsymbol{x}, \omega_0)$ for a given observed or simulated realization $\omega_0$. These modes allow us to quickly obtain information about the dynamics of this time series and then to infer simple reduced-order models for evolving the coefficients $\zeta_i(t; \omega)$ of a more general solution $\boldsymbol{u}(t, \boldsymbol{x}; \omega)$ by Galerkin projection. DMD and POD may be very useful and efficient methods to analyze the given time series $\boldsymbol{u}(t_k, \boldsymbol{x}; \omega_0)$ and infer information about its *hidden* dynamics, but the use of the inferred reduced-order model may be allowed only if the variability of the observed snapshot is sufficiently representative, in both time and stochastic domains, of the nonreduced stochastic solution $\boldsymbol{u}(t, \boldsymbol{x}; \omega)$. As will be demonstrated hereafter, the dynamically orthogonal (DO) equations overcome this difficulty as they allow us to predict *both* the variability and the time evolution of the stochastic solution $\boldsymbol{u}(t, \boldsymbol{x}; \omega)$ solely from its nonreduced dynamics.

In general, the above methods may not be well suited for capturing low-rank solutions that do not decompose on a small number of time-invariant modes (e.g., as in POD and DMD), or that exhibit spatial irregularities not easily captured by Fourier modes (e.g., as in spectral methods), or for multimodal and non-Gaussian behaviors of the coefficients (e.g., as in polynomial chaos methods). This is especially the case with material transport, as advection tends to create fine features in the solution, with sharp gradients or shocks that evolve in time and space. Capturing them requires careful numerical schemes [55, 54, 71, 48]. Upwinding, total variation diminishing (TVD), and essentially nonoscillatory (ENO) schemes use diverse rules depending on the sign of the advecting velocity. How to adapt these schemes for reduced-order numerical advection, which cannot afford examining the realizations individually, is therefore particularly challenging [77, 80, 65]. This explains in part why many stochastic advection attempts have essentially restricted themselves to 1D applications [19, 28, 13, 56] or simplified 2D cases that do not exhibit strong shocks [81].

In contrast with these reduced-order methods, the DO methodology [63, 64] solves dynamical equations to simultaneously evolve a time-dependent basis of modes, $\boldsymbol{u}_i(t, \boldsymbol{x})$, and coefficients, $\zeta_i(t; \omega)$:

$$(7) \qquad \boldsymbol{\psi}(t, \boldsymbol{x}; \omega) \simeq \sum_{i=1}^{r_\Psi} \zeta_i(t; \omega) \boldsymbol{u}_i(t, \boldsymbol{x}).$$

This dynamic approach [37] can efficiently capture the evolving spatial flow features and their variability at the minimal condition that such a modal approximation (7) exists for the nonreduced solution $\boldsymbol{\psi}(t, \boldsymbol{x}; \omega)$ [30, 52, 17]. Numerical schemes for DO equations were derived for a variety of dynamics, from stochastic Navier–Stokes [80] to Hamilton–Jacobi [74] equations. Recently, using differential geometry, the DO equations were shown [17] to be instantaneously optimal among any other reduced-order model. In fact, a nonintrusive matrix version of the DO approach was independently introduced to efficiently evolve time-dependent matrices [30]. Dynamical systems that continuously perform classic matrix operations [5, 8, 73, 12] or learn dominant Kalman filter subspaces [34, 36] have also been derived. However, critical research

questions remain for stochastic DO transports. They relate to the consistency of the direct MC integration with the numerical DO integration, to the ill-conditioning of the coefficient matrix [49] (related to the curvature of the reduced-rank manifold), to the need to capture the sharp local gradients of the advected fields, and to the issue of maintaining the numerical orthonormality of the dynamic modes.

The purpose of this article is thus to utilize the DO decomposition [63] and its geometric interpretations [17] to obtain a systematic, optimal reduced-order method for equation (6) and to derive new numerical schemes that answer the above questions for stochastic advection and Lagrangian transports. For the latter, as an immediate benefit, a novel and efficient computational methodology for evaluating an ensemble of flow-maps $\boldsymbol{\psi}(t,\boldsymbol{x};\omega) = \boldsymbol{\phi}_0^t(\boldsymbol{x};\omega)$ of the ODE (5) with random velocity is obtained. The issue of shock capturing is addressed by considering fully linear but stabilized advection schemes. This provides deterministic-stochastic consistency and compatible reduced-order schemes that rely on tensor decompositions of either the solution, $\boldsymbol{\psi}$, or its time derivative, $-\boldsymbol{v} \cdot \nabla \boldsymbol{\psi}$. The schemes obtained are not restricted to pure transport; they are also applicable to SPDEs with advection terms of the form $\boldsymbol{v} \cdot \nabla$, such as the Navier–Stokes equations.

A synopsis of the coupled DO PDEs for the dynamical evolution of the tensor decomposition (7) is given in section 2. Numerical schemes for this set of PDEs are obtained by applying the DO methodology directly to the spatial discretization of the stochastic transport PDE rather than its continuous version (6). In that framework, the DO equations find rigorous geometric justification, corresponding to optimality conditions [17, 30, 52]. Section 3 focuses on the implementation in practice of the DO machinery to solve the stochastic transport PDE (6). Factorization properties of the advection operator must be preserved at the discrete level to ensure deterministic-stochastic consistency and avoid additional approximations. This is ensured through the selection of a fully linear advection scheme whose accuracy and stability are obtained by the use of high-order spatial and temporal discretization combined with linear filtering, a technique popular in ocean modeling [68, 34]. It is explained how stochastic boundary conditions (BCs) can be accounted for by the model order reduced method in an optimal and convenient manner. Different possible time-steppings for the DO equations are discussed, as well as the issue of modifying dynamically the stochastic dimensionality $r_\Psi$ of the tensor approximation (7). Finally, as a requirement of both the DO method and multisteps time-marching schemes, an efficient method is proposed for preserving the orthonormality of the modal basis $(\boldsymbol{u}_i)$ during the time integration, as well as the smooth evolution of this basis and the coefficients $\zeta_i$. Numerical results of the overall methodology are presented in section 4 using the bidimensional stochastic analytic double-gyre flow and stochastic flow past a cylinder, both of which include sharp gradients. The DO results are finally contrasted with those of direct MC.

**Notation.** Important notation is summarized below:

| | |
|---|---|
| $\Omega \subset \mathbb{R}^d$ | Spatial domain |
| $\boldsymbol{x} \in \Omega$ | Spatial position |
| $\boldsymbol{v}(t,\boldsymbol{x};\omega)$ | Stochastic velocity field |
| $\boldsymbol{\psi}(t,\boldsymbol{x};\omega) \simeq \sum_{k=1}^{r_\Psi} \zeta_k(t;\omega)\boldsymbol{u}_k(t,\boldsymbol{x})$ | Rank-$r_\Psi$ tensor approximation of the stochastic solution of the transport PDE (6) |
| $\mathcal{M}_{l,m}$ | Space of $l$-by-$m$ real matrices |
| $\boldsymbol{\Psi}_{i,\alpha}(t) \simeq \boldsymbol{\psi}(t,\boldsymbol{x}_i;\omega_\alpha)$ | Full-rank discrete approximation $\boldsymbol{\Psi}(t) \in \mathcal{M}_{l,m}$ of the continuous solution $\boldsymbol{\psi}$ |

| | |
|---|---|
| $U_{i,k}(t) = \boldsymbol{u}_k(t, \boldsymbol{x}_i), Z_{\alpha,k}(t) = \zeta_k(t; \omega_\alpha)$ | Discrete approximation of the modes and the coefficients with $U \in \mathcal{M}_{l,r_\Psi}$, $U^T U = I$, $Z \in \mathcal{M}_{m,r_\Psi}$, and $\mathrm{rank}(Z) = r_\Psi$ |
| $\mathcal{M} = \{\Psi \in \mathcal{M}_{l,m} | \mathrm{rank}(\Psi) = r_\Psi\}$ | Fixed-rank matrix manifold |
| $\Psi(t) = U(t)Z(t)^T \in \mathcal{M}$ | Rank-$r_\Psi$ approximation of the discretized solution $\boldsymbol{\Psi}(t)$ |
| $\mathcal{T}(\Psi)$ | Tangent space at $\Psi \in \mathcal{M}$ |
| $\mathcal{N}(\Psi)$ | Normal space at $\Psi \in \mathcal{M}$ |
| $\Pi_{\mathcal{T}(\Psi)}$ | Orthogonal projection onto the plane $\mathcal{T}(\Psi)$ |
| $\Pi_{\mathcal{M}}$ | Orthogonal projection onto $\mathcal{M}$ or rank $r_\Psi$–truncated SVD |
| $I$ | Identity mapping |
| $A^T$ | Transpose of a square matrix $A$ |
| $\langle A, B \rangle = \mathrm{Tr}(A^T B)$ | Frobenius scalar product for matrices |
| $\langle \boldsymbol{u}, \boldsymbol{v} \rangle$ | $L^2$ scalar product for functions $\boldsymbol{u}, \boldsymbol{v}$ over $\Omega \subset \mathbb{R}^d$ |
| $\|A\| = \mathrm{Tr}(A^T A)^{1/2}$ | Frobenius norm |
| $\sigma_1(A) \geq \cdots \geq \sigma_{\mathrm{rank}(A)}(A)$ | Nonzero-singular values of $A \in \mathcal{M}_{l,m}$ |
| $\dot{\Psi} = \mathrm{d}\Psi/\mathrm{d}t$ | Time derivative of a rank-$r_\Psi$ solution $\Psi$ |
| $\rho_\Psi$ | Retraction on the manifold $\mathcal{M}$ at $\Psi \in \mathcal{M}$ |

## 2. Dynamically Orthogonal Stochastic Transport Equations.

**2.1. Mathematical Setting for the Transport PDE.** The stochastic transport PDE (6) is set on a smooth bounded domain $\Omega$ of $\mathbb{R}^d$, where $d$ denotes the spatial dimension. The flow-map $\boldsymbol{\phi}_0^t$ of the ODE (5) is defined for all time if particle trajectories don't leave the domain $\Omega$, which is ensured if the normal flux $\boldsymbol{v} \cdot \boldsymbol{n}$ vanishes on the boundary $\partial\Omega$, with $\boldsymbol{n}$ denoting the outward normal of $\Omega$. In the following, we deal with the more general case where $\boldsymbol{v} \cdot \boldsymbol{n}$ may have an arbitrary sign on $\partial\Omega$. Inlet and outlet boundaries are denoted, respectively, by

$$\partial\Omega_-(t; \omega) = \{x \in \partial\Omega | \boldsymbol{v}(t, x; \omega) \cdot \boldsymbol{n} < 0\},$$
$$\partial\Omega_+(t; \omega) = \{x \in \partial\Omega | \boldsymbol{v}(t, x; \omega) \cdot \boldsymbol{n} \geq 0\}.$$

Boyer [4] has shown that the transport equation (6) is well posed (under suitable regularity assumptions on $\boldsymbol{v}$), provided a Dirichlet BC is prescribed at the inlet, $\partial\Omega_-(t; \omega)$. Following Leung [44], this work considers the Dirichlet BC

$$(8) \qquad \boldsymbol{\psi}(t, \boldsymbol{x}; \omega) = \boldsymbol{x} \text{ on } \partial\Omega_-(t; \omega),$$

which ensures that the solution $\boldsymbol{\psi}(t, \boldsymbol{x}; \omega)$ carries the value of the initial entering location of the particle that arrived in $\boldsymbol{x}$ at time $t$. Theoretically, no BC is required on the outlet boundary, $\partial\Omega_+(t; \omega)$, but some conditions may be used for convenience, e.g., for numerical schemes that do not use upwinding rules. In the applications of section 4, the Neumann BC was considered:

$$(9) \qquad \frac{\partial \boldsymbol{\psi}}{\partial \boldsymbol{n}}(t, \boldsymbol{x}; \omega) = 0 \text{ on } \partial\Omega_+(t; \omega),$$

which is a BC previously implemented in [44] and which naturally arises when considering $\boldsymbol{\psi}$ as a viscous limit of equation (6) (see Theorem 4.1 in [4]). This zero normal flux condition can be interpreted as due to artificial viscosity that instantaneously diffuses trajectories normally to the outlet. For simplicity, it is assumed that a dynamic low-rank approximation of the stochastic velocity field $\boldsymbol{v}$ is available:

$$(10) \qquad \boldsymbol{v}(t, \boldsymbol{x}; \omega) = \sum_{k=1}^{r_{\boldsymbol{v}}} \beta_k(t; \omega) \boldsymbol{v}_k(t, \boldsymbol{x}),$$

which can be obtained by truncating the Karhunen–Loève expansion [58].

**2.2. The DO Field Equations.** The DO field equations evolve adaptive modes $\boldsymbol{u}_i(t, \boldsymbol{x})$ and stochastic coefficients $\zeta_i(t; \omega)$, which are both time-dependent quantities, to most accurately evolve the modal approximation (7). Such equations can formally be found by replacing the solution $\boldsymbol{\psi}$ with its tensor approximation (7) in the transport equation (6):

$$(11) \qquad (\partial_t \zeta_j) \boldsymbol{u}_j + \zeta_j \partial_t \boldsymbol{u}_j + \zeta_j \beta_k \boldsymbol{v}_k \cdot \nabla \boldsymbol{u}_j = 0,$$

where the Einstein summation convention over repeated indices is used. The family of modes is assumed orthonormal, namely,

$$(12) \qquad \forall 1 \le i, j \le r_\Psi, \quad \langle \boldsymbol{u}_i, \boldsymbol{u}_j \rangle = \int_\Omega (\boldsymbol{u}_i(t, \boldsymbol{x}), \boldsymbol{u}_j(t, \boldsymbol{x})) \mathrm{d}\boldsymbol{x} = \delta_{ij},$$

where $\langle, \rangle$ and $(,)$ denote the scalar products on $L^2(\Omega)$ and on the space $\mathbb{R}^d$, respectively. Furthermore, without loss of generality, the "DO condition"

$$(13) \qquad \forall 1 \le i, j \le r_\Psi, \quad \langle \partial_t \boldsymbol{u}_i, \boldsymbol{u}_j \rangle = 0$$

is imposed to remove the redundancy in (7), coming from the fact that the modal decomposition is invariant under rotations of modes $\boldsymbol{u}_i$ and coefficients $\zeta_i$ [63, 17]. Equations for the coefficients $\zeta_i$ are then obtained by $L^2$ projection of (11) onto the modes $\boldsymbol{u}_i$:

$$(14) \qquad \forall 1 \le i \le r_\Psi, \quad \partial_t \zeta_i + \zeta_j \beta_k \langle \boldsymbol{v}_k \cdot \nabla \boldsymbol{u}_j, \boldsymbol{u}_i \rangle = 0.$$

Governing equations for the modes $\boldsymbol{u}_i$ are obtained by $L^2$ projection on the space of the stochastic coefficients; multiplying (11) by $\zeta_i$, replacing $\partial_t \zeta_j$ using (14), yields

$$\zeta_i(-\zeta_l \beta_k \langle \boldsymbol{v}_k \cdot \nabla \boldsymbol{u}_l, \boldsymbol{u}_j \rangle) \boldsymbol{u}_j + \zeta_i \zeta_j \partial_t \boldsymbol{u}_j + \zeta_i \zeta_j \beta_k \boldsymbol{v}_k \cdot \nabla \boldsymbol{u}_j = 0,$$

which allows us to obtain, after taking the expectation and multiplying by the inverse $(\mathbb{E}[\zeta_i \zeta_j])^{-1}$ of the symmetric moment matrix $(\mathbb{E}[\zeta_i \zeta_j])_{1 \le i, j \le r_\Psi}$,

$$(15) \quad \partial_t \boldsymbol{u}_i + (\mathbb{E}[\zeta_i \zeta_j])^{-1} \mathbb{E}[\zeta_i \zeta_j \beta_k] \boldsymbol{v}_k \cdot \nabla \boldsymbol{u}_j = (\mathbb{E}[\zeta_i \zeta_j])^{-1} \mathbb{E}[\zeta_i \zeta_l \beta_k] \langle \boldsymbol{v}_k \cdot \nabla \boldsymbol{u}_l, \boldsymbol{u}_j \rangle \boldsymbol{u}_j.$$

Deriving BCs is slightly more delicate, as (8) and (9) involve a stochastic partition $\partial\Omega = \partial\Omega_-(t; \omega) \cup \partial\Omega_+(t; \omega)$ of the boundary. They are obtained again by inserting (7) into the original equations (8) and (9), which can then be rewritten as

$$\sum_{j=1}^{r_\Psi} \left[ \zeta_j \boldsymbol{u}_j \mathbf{1}_{\boldsymbol{v} \cdot \boldsymbol{n} < 0} + \zeta_j \frac{\partial \boldsymbol{u}_j}{\partial \boldsymbol{n}} \mathbf{1}_{\boldsymbol{v} \cdot \boldsymbol{n} \ge 0} \right] = \boldsymbol{x}\, \mathbf{1}_{\boldsymbol{v} \cdot \boldsymbol{n} < 0} \text{ on } \partial\Omega,$$

where $\mathbf{1}_{\boldsymbol{v} \cdot \boldsymbol{n} < 0}(t, \boldsymbol{x}; \omega)$ is the random indicator variable equal to 1 when $\boldsymbol{v} \cdot \boldsymbol{n} < 0$ and 0 otherwise, and $\mathbf{1}_{\boldsymbol{v} \cdot \boldsymbol{n} \ge 0} = 1 - \mathbf{1}_{\boldsymbol{v} \cdot \boldsymbol{n} < 0}$. Projecting again on the space of coefficients, $\zeta_i$, yields mixed BCs for the modes $\boldsymbol{u}_i$:

$$(16) \qquad \mathbb{E}[\zeta_i \zeta_j \mathbf{1}_{\beta_k \boldsymbol{v}_k \cdot \boldsymbol{n} < 0}] \boldsymbol{u}_j + \mathbb{E}[\zeta_i \zeta_j \mathbf{1}_{\beta_k \boldsymbol{v}_k \cdot \boldsymbol{n} \ge 0}] \frac{\partial \boldsymbol{u}_j}{\partial \boldsymbol{n}} = \mathbb{E}[\zeta_i \mathbf{1}_{\beta_k \boldsymbol{v}_k \cdot \boldsymbol{n} < 0}] \boldsymbol{x} \text{ on } \partial\Omega.$$

The reader is referred to [21] for further developments on DO BCs.

So far, the coupled PDEs for DO modes and coefficients (14)–(16) have been derived *first* [63, 74, 52] and numerical schemes developed thereafter [80]. In doing so,

the numerical consistency between the original SPDE (6) and the model order reduced system (14)–(16) should be respected. In addition, since unadapted discretizations of the convective terms $\boldsymbol{v} \cdot \nabla \boldsymbol{\psi}$ in (1) can lead to instability (blowing up) of the numerical solution, a great deal of attention must be paid to the discretization of the modal fluxes $\boldsymbol{v}_k \cdot \nabla \boldsymbol{u}_j$. Popular advection schemes [47, 54] utilize upwinding, in the sense that spatial derivatives are discretized according to the orientation of the full velocity, $\boldsymbol{v}$. When the velocity $\boldsymbol{v}$ becomes stochastic, this is not an issue for direct MC solutions of (6), but for reduced-order equations such as (14)–(16), special care must be taken to ensure stability without having recourse to expensive MC evaluations. These difficulties were acknowledged in previous works dealing with stochastic Navier–Stokes equations. For example, an empirical remedy consists of averaging numerical fluxes according to the probability distribution of the velocity direction [80]. In the following, it is shown that these issues can in fact be more directly addressed by using the geometric matrix framework investigated in [17].

**2.3. Geometric Framework in Matrix Spaces and Theoretical Guarantees.**
Instead of seeking numerical schemes for the continuous DO equations (14)–(16), it is numerically useful to apply the DO methodology directly on the spatial discretization chosen for the original SPDE (6). The results then indicate consistent discretizations of DO equations, assuming these are well posed, i.e., DO discretizations that still accurately simulate each discretized deterministic realization.

At the spatially discrete level, realizations of the solution vector field are represented in computer memory by the entries of an $l$-by-$m$ matrix $\boldsymbol{\Psi}_{i,j}(t) = \boldsymbol{\psi}(t, \boldsymbol{x}_i; \omega_j)$, where $l$ denotes the total spatial dimension (typically $l/d$ nodes $\boldsymbol{x}_i$ are used for a $d$-dimensional domain) and $m$ realizations $\omega_j$ are considered. The numerical solution, $\boldsymbol{\Psi}(t)$, of the SPDE (6) is obtained by solving the matrix ODE

$$\dot{\boldsymbol{\Psi}} = \mathcal{L}(t, \boldsymbol{\Psi}), \tag{17}$$

where $\mathcal{L}$ is a matrix operator that includes spatial discretizations of the realizations of the fluxes $-\boldsymbol{v} \cdot \nabla \boldsymbol{\psi}$ and of the BCs (8). In that context, model order reduction consists of approximating the solution of the large $l$-by-$m$ ODE system (17) by a low-rank decomposition

$$\boldsymbol{\Psi}(t) \simeq \Psi(t) = U(t)Z(t)^T, \tag{18}$$

similarly as in (7), where $U(t)$ and $Z(t)$ are, respectively, lower-dimensional $l$-by-$r_\Psi$ and $m$-by-$r_\Psi$ matrices containing the discretizations $U_{ik}(t) = \boldsymbol{u}_k(t, \boldsymbol{x}_i)$ and $Z_{jk}(t) = \zeta_k(t; \omega_j)$ of the modes and coefficients. The orthonormality of modes (12) and the DO condition (13) then require that the columns of $U$ be orthonormal and orthogonal to their derivatives, namely,

$$U^T U = I \text{ and } U^T \dot{U} = 0, \tag{19}$$

where $I$ is the $r_\Psi$-by-$r_\Psi$ identity matrix. In this matrix framework, the DO methodology can be rigorously formulated as a dynamical system on the manifold

$$\mathscr{M} = \{\Psi \in \mathcal{M}_{l,m} | \mathrm{rank}(\Psi) = r_\Psi\}$$

of rank-$r_\Psi$ matrices embedded in the space $\mathcal{M}_{l,m}$ of $l$-by-$m$ matrices. In what follows, the bold notation $\boldsymbol{\Psi} \in \mathcal{M}_{l,m}$ is used to refer to matrices of the ambient space $\mathcal{M}_{l,m}$ whose rank, $\mathrm{rank}(\boldsymbol{\Psi})$, is in general greater than $r_\Psi$. The nonbold notation $\Psi \in \mathscr{M}$ refers to rank-$r_\Psi$ matrices on the manifold. The DO approximation $\Psi(t)$ is defined to
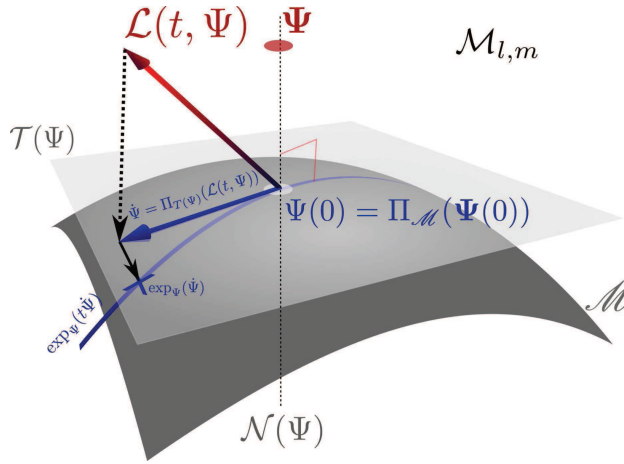
**Fig. 2** *Geometric interpretation of the DO approximation and of the exponential map* $\exp_R$*. The time derivative* $\mathcal{L}(t, R)$ *is replaced by its best tangent approximation. Schematic adapted from Wikimedia Commons, https://commons.wikimedia.org/wiki/file:tangentialvektor.svg.*

be the dynamical system on $\mathcal{M}$ geometrically obtained by replacing the vector field $\mathcal{L}(t, \cdot)$ with its tangent projection [17, 30]:

$$(20) \qquad \begin{cases} \dot{\Psi} = \Pi_{\mathcal{T}(\Psi)}(\mathcal{L}(t, \Psi)), \\ \Psi(0) = \Pi_{\mathcal{M}}(\boldsymbol{\Psi}(0)), \end{cases}$$

where the notation $\Pi_{\mathcal{M}}$ denotes the orthogonal projection onto the manifold $\mathcal{M}$ and $\Pi_{\mathcal{T}(\Psi)}$ the orthogonal projection onto its tangent space at the point $\Psi$ (see Figure 2). Given the choices (18) and (19), the ODE system (20) can be written as a set of coupled evolution equations for the mode and coefficient matrices $U$ and $Z$ that turn out to be exactly a discrete version of the continuous DO equations (14) and (15):

$$(21) \qquad \begin{cases} \dot{Z} = \mathcal{L}(t, UZ^T)^T U, \\ \dot{U} = (I - UU^T)\mathcal{L}(t, UZ^T)Z(Z^T Z)^{-1}. \end{cases}$$

The orthogonal projection $\Pi_{\mathcal{M}}$ onto $\mathcal{M}$ used for the initialization of $\Psi(0)$ is nothing more than the application that maps the matrix $\boldsymbol{\Psi}$ onto its best rank-$r_{\Psi}$ approximation, i.e., the truncated SVD [27] (this approach was used to initialize ocean uncertainty predictions [40, 38]). The SVD of the original numerical solution is the discrete analogue of the Karhunen–Loève decomposition:

$$\boldsymbol{\Psi} = \sum_{i=1}^{\text{rank}(\boldsymbol{\Psi})} \sigma_i(\boldsymbol{\Psi}) u_i v_i^T,$$

where $\sigma_1(\boldsymbol{\Psi}) \geq \cdots \geq \sigma_{\text{rank}(\boldsymbol{\Psi})}(\boldsymbol{\Psi}) > 0$ are the singular values of $\boldsymbol{\Psi}$, and $u_i$ and $v_i$ are orthonormal families of left and right singular vectors. The truncated SVD is the algebraic operation that removes modes of order higher than $r_{\Psi}$:

$$(22) \qquad \Pi_{\mathcal{M}}(\boldsymbol{\Psi}) = \sum_{i=1}^{r_{\Psi}} \sigma_i(\boldsymbol{\Psi}) u_i v_i^T \in \mathcal{M}.$$

Feppon and Lermusiaux [17] have shown that the dynamical system (20) instantaneously applies the truncated SVD to constrain the rank of the reduced solution $\Psi$ at

all times. In other words, it is the continuous limit when $\Delta t \to 0$ of the solution that would be obtained by systematically applying the truncated SVD after any Euler (or any other explicit time discretization) time step:

$$(23) \qquad \Pi_{\mathcal{T}(\Psi)}(\mathcal{L}(t,\Psi)) = \lim_{\Delta t \to 0} \frac{\Pi_{\mathcal{M}}(\Psi + \Delta t \mathcal{L}(t,\Psi)) - \Psi}{\Delta t}.$$

Therefore, (20) yields an optimal time evolution of the modal decomposition $\Psi = UZ^T$ at least for small integration times. More theoretical guarantees have been obtained in [17], where it is proven that the error of the DO approximation (20) is controlled by the best truncation error $\|\Psi(t) - \Pi_{\mathcal{M}}(\Psi(t))\|$ as long as the original solution $\Psi(t)$ remains at a close distance from the set $\mathcal{M}$ of low-rank matrices, which translates into the algebraic condition

$$\sigma_{r_\Psi}(\Psi(t)) > \sigma_{r_\Psi+1}(\Psi(t));$$

i.e., singular values of order $r_\Psi$ and $r_\Psi+1$ do not cross (a condition previously observed numerically in [30, 52]).

**3. Implementation of the DO Approximation for Stochastic Advection.** Exploiting the geometric framework, new schemes for the DO approximation (21) of the stochastic transport equation (6) are obtained. High-order linear stabilized advection schemes that maintain sharp spatial gradients and deterministic-stochastic consistency are presented (subsection 3.1). Stochastic DO BCs derived from optimality criteria are discussed (subsection 3.2). Time-marching strategies for the DO equations, using the truncated SVD and the retractions [1] for maintaining the numerical solution on the low-rank manifold, are obtained and contrasted: direct Euler, exponential map from geodesic equations, and algebraic and gradient descent–based time-marching (subsection 3.3). Finally, accurate methods for dynamically evolving the rank of the DO subspace and for preserving the orthonormality of the modes and their smooth evolution are derived (subsections 3.4 and 3.5).

**3.1. Motivations for Linear Advection Schemes.** The DO approximation is computationally attractive because (21) evolves a solution constrained to the low-rank manifold of small dimension $(l+m)r_\Psi - r_\Psi{}^2$ (by evolving the $lr_\Psi + mr_\Psi$ coefficients of the matrices $U$ and $Z$ with $U$ orthonormal), instead of the initial $lm$ independent matrix coefficients of the original high-dimensional dynamical system (17). As a consequence, the DO matrix system (21) offers a true gain of computational efficiency *only* if the evaluation of $l$-by-$m$ matrices can be avoided. This is not a priori achievable in a direct nonintrusive scheme if the operator $\mathcal{L}$ needs to be evaluated on the $l$-by-$m$ matrix $\Psi = UZ^T$. If all $lm$ coefficients of $\Psi$ were needed to be computed from $U$ and $Z$, there would be no computational benefit other than a reduction of memory storage in comparison with solving the original nonreduced system (17). The gain of efficiency can be achieved if the operator $\mathcal{L}(t,\cdot)$ maps a rank-$r_\Psi$ decomposition $\Psi = UZ^T$ onto a factorization

$$(24) \qquad \mathcal{L}(t, UZ^T) = L_U L_Z^T$$

of rank at most $r_L$, where $L_U$ is an $l$-by-$r_L$ matrix, $L_Z$ an $m$-by-$r_L$ matrix, and $r_L$ an integer typically largely inferior to $l$ and $m$. In that case, the system (21) can be computed efficiently as

$$(25) \qquad \begin{cases} \dot{Z} = L_Z[L_U^T U], \\ \dot{U} = [(I - UU^T)L_U][L_Z^T Z(Z^T Z)^{-1}], \end{cases}$$

where brackets have been used to highlight products that allow us to compute the derivatives $\dot{U}$ and $\dot{Z}$ without having to deal with $l$-by-$m$ matrices. Such factorization occurs for instance when $\mathcal{L}(t, \cdot)$ is polynomial of order $d$, for which rank-$r_\Psi$ matrices are mapped onto rank-$r_L \leq (r_\Psi)^d$ matrices.

From the spatially continuous viewpoint, the differential operator $\boldsymbol{\psi} \mapsto \boldsymbol{v} \cdot \nabla \boldsymbol{\psi}$ satisfies this condition, as the rank-$r_\Psi$ decomposition (7) is mapped to one of rank $r_L = r_\Psi \times r_{\boldsymbol{v}}$:

$$
(26) \qquad \boldsymbol{v} \cdot \nabla \boldsymbol{\psi} = \sum_{\substack{1 \leq j \leq r_\Psi \\ 1 \leq k \leq r_{\boldsymbol{v}}}} \zeta_j \beta_k \boldsymbol{v}_k \cdot \nabla \boldsymbol{u}_j.
$$

This equation further highlights why adapting advection schemes to model order reduction is challenging, as popular discretizations of $\boldsymbol{v} \cdot \nabla \boldsymbol{\psi}$ involve nonpolynomial nonlinearities in the matrix operator $\mathcal{L}$. These schemes rely indeed on the use of min-max functions required by upwinding or high-order discretizations such as ENO or TVD schemes that select a smooth approximation of the spatial derivative $\nabla \boldsymbol{\psi}$, e.g., [77]. In these cases, the nonlinearity of the operator $\mathcal{L}$ prevents the decomposition (26) from holding at the discrete level without introducing further approximations, which may drastically alter the stability of time integration and the accuracy of the numerical solution. A very natural approach followed by [63, 80] is to assume that the decomposition (26) holds before applying nonlinear schemes to discretize the fluxes $\boldsymbol{v}_k \cdot \nabla \boldsymbol{u}_j$ in (14) and (15). A key issue then is to maintain consistency between the deterministic MC and stochastic DO solutions. Indeed, in the examples considered in section 4, for which high gradients occur, such approaches were at times observed to lead to either numerical explosion or significant errors for long integration times.

Consequently, this work investigated the use of linear central advection schemes that do not require upwinding and that have the property of preserving the decomposition (26). Therefore, the advection $-\boldsymbol{v} \cdot \nabla \boldsymbol{\psi}$ is discretized as

$$
(27) \qquad \mathcal{L}(t, \boldsymbol{\Psi})_{i,\alpha} = -\boldsymbol{v}(t, \boldsymbol{x}_i; \omega_\alpha) \cdot \mathrm{D} \boldsymbol{\Psi}_{i,\alpha},
$$

where D is a linear finite-difference operator approximating the gradient $\nabla$. With $\Psi = U Z^T$ as in (18), this yields the decomposition $\mathcal{L}(t, \Psi) = L_U L_Z^T$, as required in (25), where $L_U$ and $L_Z$ are the $l$-by-$r_L$ and $m$-by-$r_L$ matrices

$$
(L_U)_{i,jk} = \boldsymbol{v}_k(t, \boldsymbol{x}_i) \cdot \mathrm{D} \boldsymbol{u}_j(t, \boldsymbol{x}_i), \quad (L_Z)_{\alpha, jk} = \zeta_j(t; \omega_\alpha) \beta_k(t, \omega_\alpha).
$$

In one dimension, the gradient can be approximated by the second-order operator

$$
(28) \qquad \mathrm{D} \boldsymbol{\Psi}_{i,\alpha} = \frac{\boldsymbol{\Psi}_{i+1,\alpha} - \boldsymbol{\Psi}_{i-1,\alpha}}{2\Delta x},
$$

and this article will also consider the sixth-order finite-difference operator

$$
(29) \qquad \mathrm{D} \boldsymbol{\Psi}_{i,\alpha} = \frac{3}{2} \frac{\boldsymbol{\Psi}_{i+1,\alpha} - \boldsymbol{\Psi}_{i-1,\alpha}}{2\Delta x} - \frac{3}{5} \frac{\boldsymbol{\Psi}_{i+2,\alpha} - \boldsymbol{\Psi}_{i-2,\alpha}}{4\Delta x} + \frac{1}{10} \frac{\boldsymbol{\Psi}_{i+3,\alpha} - \boldsymbol{\Psi}_{i-3,\alpha}}{6\Delta x},
$$

where $\Delta x$ denotes the spatial resolution, and a natural numbering is assumed for the index $i$. These formulas are adapted in a straightforward manner to discretize partial derivatives in higher dimension [54]. This approach might seem unexpected, since central schemes are known to be numerically unstable under Euler time integration. In addition, the Godunov theorem says that it is not possible to devise a linear

scheme higher than first-order accuracy that does not create false extrema in numerical solutions [18]. These extrema are produced by numerical dispersion and manifest in the form of spurious oscillations. In fact, it is possible to contain this phenomenon near shocks and obtain high-order accuracy where the solution is smooth. Stability and the removal of part of the oscillations can be achieved by introducing the right amount of numerical dissipation, using either artificial viscosity [72] or filtering [68, 14, 32, 59, 11]. Shapiro filters are especially attractive because they are easy to implement, fully linear, and designed to optimally remove the shortest resolvable numerical frequency without affecting other wave components [68, 69, 70]. In one dimension, setting $\delta^2$ as the operator $\delta^2 \Psi_{i,\alpha} = \Psi_{i+1,\alpha} - 2\Psi_{i,\alpha} + \Psi_{i+1,\alpha}$, the Shapiro filters $\mathcal{F}^{(i)}$ of order $i = 2$, 4, and 8 are defined by the formulas (see [68])

$$
(30) \quad \begin{aligned}
\mathcal{F}^{(2)} \Psi_{i,\alpha} &= (1 + \delta^2/4)\Psi_{i,\alpha}, \\
\mathcal{F}^{(4)} \Psi_{i,\alpha} &= (1 - \delta^2/4)(1 + \delta^2/4)\Psi_{i,\alpha}, \\
\mathcal{F}^{(8)} \Psi_{i,\alpha} &= (1 + \delta^4/16)(1 - \delta^4/16)\Psi_{i,\alpha}.
\end{aligned}
$$

The order and frequency of applications can be tuned to the desired filter spectrum [34]. Their linearity allows us to filter the decomposition $\boldsymbol{\psi} = \zeta_i \boldsymbol{u}_i$ efficiently by filtering the discretization of the modes $\boldsymbol{u}_i$ or, in other words, $\mathcal{F}^{(i)}(UZ^T) = (\mathcal{F}^{(i)}U)Z^T$. Critically, this DO filtering is consistent with the filtering of MC realizations.

To achieve further stability, higher-order discretizations of the temporal derivative are generally used to complement these filters. Popular linear multistep methods are leapfrog [83], Runge–Kutta, and Adam Bashforth [11]. For instance, for a time increment $\Delta t$, the second-order leapfrog scheme evolves the value $\boldsymbol{\Psi}^n$ of the numerical solution $\boldsymbol{\Psi}$ at time $t^n = n\Delta t$ according to the rule

$$
(31) \quad \frac{\boldsymbol{\Psi}^{n+1} - \boldsymbol{\Psi}^{n-1}}{2\Delta t} = \mathcal{L}(t^n, \boldsymbol{\Psi}^n),
$$

while the third-order Runge–Kutta (RK3) method uses

$$
(32) \quad \frac{\boldsymbol{\Psi}^{n+1} - \boldsymbol{\Psi}^n}{\Delta t} = \frac{k_1^n + 4k_2^n + k_3^n}{6} \quad \text{with} \quad \begin{cases} k_1^n = \mathcal{L}(t^n, \boldsymbol{\Psi}^n), \\ k_2^n = \mathcal{L}\left(t^n + \Delta t/2, \boldsymbol{\Psi}^n + k_1^n \Delta t/2\right), \\ k_3^n = \mathcal{L}(t^n + \Delta t, \boldsymbol{\Psi}^n + \Delta t(2k_2^n - k_1^n)). \end{cases}
$$

A comparison of several combinations of these techniques is illustrated in Figure 3 for the 1D advection equation $\partial_t \psi + v \partial_x \psi = 0$, a benchmark case for selecting an appropriate linear scheme for the transport equation (6) in higher dimension. A boxcar function is advected to the right with velocity $v = 0.7$ in the domain $[0, 1]$ until time $t = 10$. The spatial resolution is set to $\Delta x = 0.002$, and the CFL condition $\Delta t \leq 0.6 v \Delta x$ is used to define the time increment $\Delta t$. The figure illustrates how accuracy and stability can be achieved by (i) using multistep time-marching schemes, (ii) using high-order spatial discretization, and (iii) adding the proper amount of numerical dissipation to remove spurious oscillations. We note that linear limiters may also be combined with Shapiro filters [24], maintaining consistency.

**3.2. Boundary Conditions.** BCs of the reduced solution were formally obtained in section 2. They could be treated more rigorously by incorporating the original BCs, (8) and (9), directly within the discretization of the operator $\mathcal{L}$. However, this approach can lead to a more complex implementation. In this work, boundary nodes are stored in an $l_{bc}$-by-$m$ "ghost" matrix, and it is assumed that the $l$-by-$m$ matrix of realizations $\boldsymbol{\Psi}$ contains only the values at internal nodes. These ghost cells allow

(a) Leapfrog, 2nd order

(b) Leapfrog, 2nd order, Shapiro filter [1,1]

(c) Leapfrog, 2nd order, Shapiro filter [1,2]

(d) RK3, 2nd order

(e) RK3, 6th order

(f) RK3, 6th order, Shapiro filter [10,3]
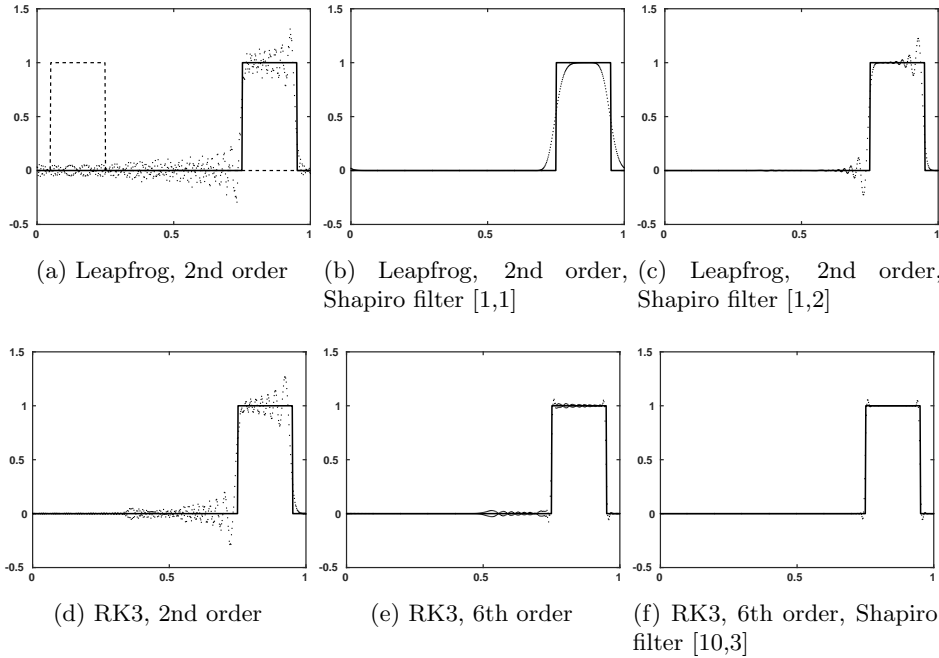
**Fig. 3** *Comparison of the numerical solution (*dotted line*) with the analytical solution (*solid line*) of the 1D advection equation for different time-integration, linear centered schemes, and filter order (specifics given in each panel caption). The text "Shapiro filter $[n_1, n_2]$" indicates that the Shapiro filter of order $2^{n_2}$ (see [68]) has been applied after every $n_1$ iterations. The initial boxcar function is visible in the dashed line on the first plot.*

convenient evaluation of the differential operator D in the definition (27) of $\mathcal{L}(t, \boldsymbol{\Psi})$. Their values are reinitialized at the beginning of each time step according to the BCs (8) and (9). In the following, the operator which assigns the values of these boundary cells at time $t$ is denoted $\mathcal{B}_C(t, \cdot)$; i.e., the discrete BCs are then explicit (if implicit, they are solved for simultaneously with the interior solution, e.g., see [21]). With this notation, the solution that includes both internal nodes and boundary values is the block matrix $\boldsymbol{\Psi}_{bc} = \left[ \begin{smallmatrix} \mathcal{B}_C(t,\Psi) \\ \Psi \end{smallmatrix} \right]$. For example, on the 1D domain $\Omega = [0, 1]$, the value of the boundary node $\boldsymbol{x}_1 = 0$ is determined by the relation

$$\mathcal{B}_C(t, \boldsymbol{\Psi})_{1,\alpha} = \begin{cases} 0 & \text{if } \boldsymbol{v}(t, 0; \alpha) \geq 0, \\ (18\boldsymbol{\Psi}_{2,\alpha} - 9\boldsymbol{\Psi}_{3,\alpha} + 2\boldsymbol{\Psi}_{4,\alpha})/11 & \text{if } \boldsymbol{v}(t, 0; \alpha) < 0, \end{cases}$$

if one uses a third-order reconstruction for the Neumann BC (9). The difficulty of determining how these BCs should be accounted for by the reduced solution $\Psi = UZ^T$ comes from the fact that assigning boundary values does not in general preserve the rank; i.e., rank$(\boldsymbol{\Psi}_{bc}) > r_\Psi$ (in practice, the rank of this interior+boundary DO solution should be large enough to represent both the reduced interior solution and the reduced BCs; see [21]). BCs may be enforced on the reduced solution while ensuring minimal error by solving the minimization problem

$$(33) \qquad \min_{\text{rank}(\Psi_{bc})=r_\Psi} \left\| \Psi_{bc} - \begin{bmatrix} \mathcal{B}_C(t, \Psi) \\ \Psi \end{bmatrix} \right\|^2.$$

This yields the best rank-$r_\Psi$ approximation of the $(l + l_{bc})$-by-$m$ matrix $\mathbf{\Psi}_{bc}$, whose decomposition $\Psi_{bc} = U_{bc}Z_{bc}^T$ allows us to conveniently compute the discrete differential operator D in (27) requiring boundary values. The minimization can, e.g., be achieved by using a gradient descent starting from the initial rank-$r_\Psi$ matrix $\Psi$, as explained in the next subsection and in [17, 50].

When BCs are deterministic or homogeneous, they can be directly implemented as BCs for the discretization of the modes $\boldsymbol{u}_i$ [63]. For example, zero Dirichlet or Neumann BCs for all the realizations of $\boldsymbol{\psi}$ directly corresponds to the same BCs for the modes $\boldsymbol{u}_i$. For more general cases, it is usually desirable to avoid solving (33) and to instead obtain BCs for the modes that optimally approximate the original BCs. This is achieved by replacing the minimization problem (33) with that for the $l_{bc}$-by-$r_\Psi$ ghost matrix $U_{bc}$ containing boundary values for the matrix $U$:

$$(34) \qquad \min_{U_{bc} \in \mathcal{M}_{l_{bc}, r_\Psi}} ||U_{bc}Z^T - \mathcal{B}_C(t, \Psi)||^2.$$

The solution of this linear regression problem is easily obtained by writing the stationarity condition

$$\forall \delta U \in \mathcal{M}_{l_{bc}, r_\Psi}, \quad 2\langle (\delta U)Z^T, U_{bc}Z^T - \mathcal{B}_C(t, \Psi) \rangle = 0,$$

which eventually yields

$$(35) \qquad U_{bc} = \mathcal{B}_C(t, \Psi)Z(Z^TZ)^{-1}.$$

It turns out that this optimality condition is the discrete analogues of the original BCs (16) obtained formally in section 2. The decomposition of the reduced solution including boundary values is therefore $\Psi_{bc} = \begin{bmatrix} U_{bc} \\ U \end{bmatrix} Z^T$. Further discussions on DO BCs are provided in [21].

**3.3. Low-Rank Time-Stepping.** One issue commonly encountered in the time discretization of dynamical systems is the fact that the discrete time-stepping tends to make the numerical solution exit the manifold $\mathscr{M}$ where the trajectories live. If $\Psi^n$ is a point on the manifold $\mathscr{M}$ at $t^n$, and $\dot{\Psi}^n \in \mathcal{T}(R)$ is the time derivative, any straight move, $\Psi^n + \Delta t \dot{\Psi}^n$, leaves the fixed-rank manifold $\mathscr{M}$. An application, called *retraction*, must be used to convert the tangent direction $X = \Delta t \dot{\Psi}^n \in \mathcal{T}(\Psi^n)$ into a point $\rho_{\Psi^n}(X)$ back onto the manifold. A retraction $\rho_{\Psi^n} : \mathcal{T}(\Psi^n) \to \mathscr{M}$ (Figure 2) is an application describing how to move on the manifold in a tangent direction $X \in \mathcal{T}(\Psi^n)$ starting from $\Psi^n \in \mathscr{M}$. By definition, it must satisfy the consistency conditions that (i) zero velocity results in a null move, i.e., $\rho_{\Psi^n}(0) = \Psi^n$, and (ii) a move in the $X$ direction results in a trajectory on $\mathscr{M}$ with $X$ as initial speed: $\frac{d}{dt}\rho_{\Psi^n}(tX)\big|_{t=0} = X$ (see [1]). The ideal retraction is the *exponential map* that follows geodesics or shortest paths on the manifold but may be expensive to evaluate. In practice, one uses approximations of this map, leading to several strategies of implementation for the explicit discretization of (21).

**3.3.1. Direct Time-Marching Scheme for the Matrix DO System (21).** As in [80, 52], a very intuitive idea for moving a rank-$r_\Psi$ matrix $\Psi^n = U^n Z^{nT}$ onto a direction $\dot{\Psi}^n = \dot{U}^n Z^{nT} + U^n \dot{Z}^{nT}$ with a step $\Delta t$ is to independently update the mode and coefficient matrices $U^n$ and $Z^n$ by using the following scheme, which is a direct Euler time discretization of the system (21):

$$(36) \qquad \begin{cases} Z^{n+1} = Z^n + \Delta t \dot{Z}^n, \\ U^{n+1} = U^n + \Delta t \dot{U}^n, \end{cases}$$

where $\dot{Z}^n$ and $\dot{U}^n$ are the approximations of the time derivatives $\dot{U}$ and $\dot{Z}$ being used. This corresponds to using the retraction $\rho_{UZ^T}$ defined by

$$(37) \quad \rho_{UZ^T}(\dot{U}Z^T + U\dot{Z}^T) = (U + \dot{U})(Z + \dot{Z})^T = UZ^T + (\dot{U}Z^T + U\dot{Z}^T) + \dot{U}\dot{Z}^T.$$

**3.3.2. The Exponential Map: Geodesic Equations between Time Steps.** The ideal retraction is the exponential map $\rho_{\Psi^n} = \exp_{\Psi^n}$ (see [1]) computed from geodesic paths $\gamma(s)$ on $\mathscr{M}$, which are the direct analogues of straight lines onto curved manifolds. These curves, parametrized as $\gamma(s) = \exp_{\Psi^n}(s\dot{\Psi}^n)$ (see Figure 2), indicate the shortest way to "walk" onto the manifold from $\Psi^n$ in the straight direction $\dot{\Psi}^n = \dot{U}^n(Z^n)^T + U^n(\dot{Z}^n)^T$. The value of $\exp_{\Psi^n}(s\dot{\Psi}^n)$ is given by the solution $\gamma(s) = U(s)Z(s)^T$ at time $s$ of the geodesic equations [17]:

$$(38) \quad \begin{cases} \ddot{Z} - Z\dot{U}^T\dot{U} = 0, \\ \ddot{U} + U\dot{U}^T\dot{U} + 2\dot{U}\dot{Z}^TZ(Z^TZ)^{-1} = 0, \\ U(0) = U^n,\ Z(0) = Z^n, \\ \dot{U}(0) = \dot{U}^n,\ \dot{Z}(0) = \dot{Z}^n. \end{cases}$$

Without direct analytical solutions to (38), numerical schemes are used. Computing retractions that approximate the exponential map well is a challenge commonly encountered in optimization on matrix manifolds with orthogonality constraints [50], as discussed in [1]. One can show that the retraction $\rho_{UZ^T}$ of equation (37) approximates the exponential map only to first order (see [1]), which can lead to numerical errors at locations of high curvature on the manifold $\mathscr{M}$. The curvature of the rank-$r_\Psi$ manifold $\mathscr{M}$ at the point $\Psi^n$ is inversely proportional to the lowest singular value $\sigma_{r_\Psi}(\Psi^n)$ [17]. As a consequence, errors can be incurred by the direct time-stepping (36) when the matrix $Z^n$ is ill conditioned. Equations (38) can be solved during the DO time integration between time steps to move more accurately on the manifold without needing to recompute values of the operator $\mathcal{L}$. For instance, Euler steps (36) can be replaced with

$$(39) \quad U^{n+1}(Z^{n+1})^T = \exp_{\Psi^n}(\Delta t \dot{\Psi}^n).$$

This can be done using high-order time-marching schemes for the discretization of (38). The intermediate time step $\delta t < \Delta t$ for these can be set adaptively: a rule of thumb is to use steps in the ambient space having a length less than the minimal curvature radius $\sigma_{r_\Psi}(Z)$ at the point $UZ^T$:

$$\delta t \|\dot{U}Z^T + U\dot{Z}^T\| < C\sigma_{r_\Psi}(Z),$$

where $C \simeq 1$ is a constant set by the user. Note that a lower-order retraction such as (37) is commonly used anyway in the time discretization of the geodesic equations (38).

**3.3.3. Direct Computation of the Truncated SVD at the Next Time Step.** As highlighted in section 2, DO equations (25) define a dynamical system that truncates the SVD at all instants to optimally constrain the rank of the reduced solution (23). Denoting $\Psi^n = U^n(Z^n)^T$ as the DO solution at time $t^n$, integrating the nonreduced dynamical system (17) for a time step $[t^n, t^{n+1}]$ yields a rank-$r_{\overline{L}} > r_\Psi$ prediction

$$(40) \quad \boldsymbol{\Psi}^{n+1} = \Psi^n + \Delta t \overline{\mathcal{L}(t^n, \Psi^n)},$$

where $\overline{\mathcal{L}(t^n, \Psi^n)}$ represent the full-space integral for the exact integration or the increment function for a numerical integration. For the latter, it can be an approximation of the time derivative $\mathcal{L}(t^n, \Psi(t^n))$, e.g., $\overline{\mathcal{L}(t^n, \Psi^n)} = \mathcal{L}(t^n, \Psi^n)$ for explicit Euler.

One way to proceed to evolve the low-rank approximation $\Psi^n$ to $\Psi^{n+1}$ is to directly compute the rank-$r_\Psi$ SVD truncation $\Pi_{\mathscr{M}}(\Psi^{n+1})$ (equation (22))

$$(41) \qquad \Psi^{n+1} = U^{n+1}(Z^{n+1})^T = \Pi_{\mathscr{M}}(\Psi^n + \Delta t \overline{\mathcal{L}(t^n, \Psi^n)})$$

to obtain modes and coefficients $U^{n+1}$ and $Z^{n+1}$ at time $t^{n+1} = t^n + \Delta t$. This scheme has been shown to be a consistent time discretization of the DO equations (20) (see [17]). For an Euler step, it corresponds to using the retraction $\rho_\Psi(X) = \Pi_{\mathscr{M}}(\Psi + X)$, a second-order accurate approximation of the exponential map [1] and hence an improvement of the direct Euler time-marching (36).

**a. Algebraically Computing the Truncated SVD.** The scheme (41) can be computed efficiently and in a fully algebraic manner when the operator $\mathcal{L}$ factors as (24). Indeed, the linear approximation of the time derivative then admits a decomposition $\overline{\mathcal{L}(t^n, U^n(Z^n)^T)} = L_U^n(L_Z^n)^T$ of rank at most $r_{\overline{L}} = r_L \times p_t$, $p_t$ being the order of the time integration scheme utilized. Therefore, $\Psi^{n+1}$ factors as

$$(42) \qquad \begin{aligned} \Psi^{n+1} &= U^n(Z^n)^T + \Delta t L_U^n(L_Z^n)^T \\ &= \Psi_U^{n+1}(\Psi_Z^{n+1})^T, \text{ with } \Psi_U^{n+1} = [U^n \ L_U^n] \text{ and } \Psi_Z^{n+1} = [Z^n \ \Delta t L_Z^n], \end{aligned}$$

with $L_U^n \in \mathcal{M}_{l,r_{\overline{L}}}, L_Z^n \in \mathcal{M}_{m,r_{\overline{L}}}$. The rank of $\Psi^{n+1}$ is therefore at most $\text{rank}(\Psi^{n+1}) = r_\Psi < r_\Psi + r_{\overline{L}}$, which can be assumed to be largely inferior to $l$ and $m$. This can be exploited to compute the truncated SVD through an algorithm that avoids computing large matrices of size $l$-by-$m$ (see Algorithm 3.1a).

---

**Algorithm 3.1a** Rank-$r_\Psi$ truncated SVD of $\Psi = \Psi_U \Psi_Z^T$ with $\Psi_U \in \mathcal{M}_{l,r_\Psi}, \Psi_Z \in \mathcal{M}_{m,r_\Psi}$ and $r_\Psi < r_\Psi = \text{rank}(\Psi) \ll \min(l,m)$

---

1: Orthonormalize the columns of the matrix $\Psi_U$ (see the discussion in subsection 3.5), i.e., find a basis change matrix $A \in \mathcal{M}_{r_\Psi, r_\Psi}$ such that $(\Psi_U A)^T(\Psi_U A) = I$ and set

$$\Psi_U \leftarrow \Psi_U A, \ \Psi_Z \leftarrow \Psi_Z A^{-T}$$

to preserve the product $\Psi = \Psi_U \Psi_Z^T$.

2: Compute the "compact" SVD of the *smaller* $m$-by-$r_\Psi$ matrix $\Psi_Z$:

$$\Psi_Z = V\Sigma P^T,$$

where $\Sigma$ is an $r_\Psi$-by-$r_\Psi$ diagonal matrix of singular values, and $V \in \mathcal{M}_{m,r_\Psi}$ and $P \in \mathcal{M}_{r_\Psi, r_\Psi}$ are orthogonal matrices of singular vectors. This is achieved by computing the eigendecomposition of the "covariance" matrix $\Psi_Z^T \Psi_Z$.

3: The SVD of $\Psi = \Psi_U \Psi_Z^T$ is given by $\Psi = U\Sigma V^T$, with $U = \Psi_U P$ an orthogonal $l$-by-$r_\Psi$ matrix of left singular vectors. The truncated SVD of order $r_\Psi$ is straightforwardly obtained from the first $r_\Psi$ columns of $U, V$, and $\Sigma$.

---

This first algorithm has some issues. First, reorthonormalizations and eigenvalue decompositions such as in steps 1 and 2 do not allow us to keep track of the smooth evolution of the mode $U(t)$ and coefficient $Z(t)$ solutions of the system (21). Additional procedures are needed [80, 79]. Second, with the repeated use of such algebraic operations, additional round-off errors may be introduced.

**b. Using Gradient Descent for Continuous Updates of the Truncated SVD.**
Alternatively, a gradient descent on the low-rank manifold $\mathscr{M}$ can be used to find the correction that needs to be added to modes $U^n$ and coefficients $Z^n$ to evaluate the SVD truncation $\Psi^{n+1} = \Pi_{\mathscr{M}}(\Psi^{n+1})$ ((41) and (42)). Indeed, $\Psi^{n+1} = U^{n+1}(Z^{n+1})^T$ (eq. (41)) is the minimizer of

$$J(UZ^T) = \frac{1}{2}||\mathbf{\Psi}_U^{n+1}(\mathbf{\Psi}_Z^{n+1})^T - UZ^T||^2,$$

where $|| \cdot ||$ is the Frobenius norm. The (covariant) gradient $\nabla J$ used for this minimization must be aligned with the maximum ascent direction tangent to $\mathscr{M}$ at $UZ^T$. Its value can be shown to be $\nabla J = (\nabla J_U)Z^T + U(\nabla J_Z)^T$ (see [17]), where $\nabla J_U$ and $\nabla J_Z$ provide respective ascent directions for the individual matrices $U$ and $Z$. Their expression and the resulting gradient descent toward the updated truncated SVD $U^{n+1}(Z^{n+1})^T$ starting from the approximate initial guess $\Psi^n = U^n(Z^n)^T$ are detailed in Algorithm 3.1b. Note that [17] proved that the procedure is convergent for almost every initial data point. If, in addition, $\Delta t$ is small enough, the method is expected to converge after only a small number of iterations, while preserving the continuous evolution of the mode and coefficient matrices $U$ and $Z$. In comparison with the use of geodesics, this method ensures the accuracy of the reduced solution while being less sensitive to the singularity of the matrix $Z$. Also, it is a direct extension of the DO time stepping (36), as one step of (36) coincides with the first step of the gradient descent (43) starting from the current value $U^n(Z^n)^T$ and with $\mu = 1$ [17].

---

**Algorithm 3.1b** Gradient descent for updating a rank-$r_\Psi$ truncated SVD of $\mathbf{\Psi} = \mathbf{\Psi}_U\mathbf{\Psi}_Z^T$ with $\mathbf{\Psi}_U \in \mathcal{M}_{l,r_\Psi}$, $\mathbf{\Psi}_Z \in \mathcal{M}_{m,r_\Psi}$, and $r_\Psi < r_\mathbf{\Psi} = \mathrm{rank}(r_\mathbf{\Psi}) \ll \min(l,m)$

1: Initialize a rank-$r_\Psi$ guess $U_0 Z_0^T \simeq \mathbf{\Psi}$ with $U_0 \in \mathcal{M}_{l,r_\Psi}, Z_0 \in \mathcal{M}_{m,r_\Psi}, U_0^T U_0 = I$.
2: To minimize $J(U,Z) = J(UZ^T) = ||\mathbf{\Psi} - UZ^T||$ on $\mathscr{M}$, compute the gradient step

$$(43) \qquad \begin{cases} Z_{k+1} = Z_k - \mu \nabla J_U(U_k, Z_k), \\ U_{k+1} = U_k - \mu \nabla J_Z(U_k, Z_k), \end{cases}$$

where $\mu$ is a small enough constant set by the user and the gradients $(\nabla J_U, \nabla J_Z)$ are given by (see Proposition 36 in [17])

$$(44) \qquad \begin{cases} \nabla J_Z(U,Z) = Z - \mathbf{\Psi}_Z[(\mathbf{\Psi}_U)^T U], \\ \nabla J_U(U,Z) = -(I - UU^T)\mathbf{\Psi}_U[(\mathbf{\Psi}_Z)^T Z(Z^T Z)^{-1}], \end{cases}$$

where brackets highlight matrix products that render the computation efficient.
3: Orthonormalize the modes $U_{k+1}$ (see subsection 3.5) after each iteration and repeat steps 2–3 until convergence is achieved.

---

**3.4. Dynamically Increasing the Rank of the Approximation.** In the SPDE (6), all realizations of the solution share the initial value $\boldsymbol{\psi}(0, \boldsymbol{x}; \omega) = \boldsymbol{x}$. Hence, the DO approximation coincides with the exact solution at time $t = 0$ and is given by the rank-one decomposition $\Psi = UZ^T$, where $U$ is a normalized column vector proportional to the discretization of the coordinate function $\boldsymbol{x}$ and $Z$ is a column vector identically equal to the normalization factor. Obviously, $\boldsymbol{\psi}(t, \boldsymbol{x}; \omega)$ becomes random after $t > 0$ and hence the rank of the DO solution must be increased immediately [64, 80] and modified dynamically to capture dominant stochastic subspaces that are

forming throughout the time evolution of the solution. This is a common issue in model order reduction of SPDEs.

Reducing the dimension $r_\Psi$ of the DO stochastic subspace is straightforward: it is sufficient to truncate the SVD of the current DO solution $\Psi = UZ^T$, using, i.e., Algorithm 3.1a, when the lowest singular value $\sigma_{r_\Psi}(\Psi) < \underline{\sigma}$ becomes lower than a threshold $\underline{\sigma}$ [64]. Increasing the stochastic dimension from $r_\Psi$ to $r_\Psi' > r_\Psi$ is more involved, as $r_\Psi' - r_\Psi$ new dominant directions $\boldsymbol{u}_i$ supporting the decomposition (7) must be found. The overall topic is linked to breeding schemes [29]; directions of maximum error growth, e.g., [57]; and nonnormal modes [16, 15, 51], but our emphasis here is on accurately capturing the present and evolving dominant uncertainties in the SVD sense, as in [43, 35, 64]. One approach [64] assumes that uncertainties are small and uniform in the orthogonal complement of the present DO subspace and then adds modes aligned with the most sensitive directions of the operator $\mathcal{L}$ in this complement, if their growth is fast enough. This computation is based on the gradient of $\mathcal{L}$ in the ambient space $\mathcal{M}_{l,m}$, and MC perturbations, but it does not guarantee tracking the best rank-$r_\Psi'$ approximation at the next time step. An additional difficulty lies in the issue of detecting when the dimension of the DO subspace should be increased. Sapsis and Lermusiaux [64] suggested increasing the rank $r_\Psi$ when $\sigma_{r_\Psi}(\Psi) > \overline{\sigma}$ reaches another threshold, $\overline{\sigma} > \underline{\sigma}$.

These issues can be resolved by examining the component of the time derivative, $\mathcal{L}(t, \Psi)$, that is normal to the manifold, i.e., $N(UZ^T) = (I - \Pi_{\mathcal{T}(UZ^T)})(\mathcal{L}(t, UZ^T)) \in \mathcal{N}(\Psi)$, and neglected by the DO approximation (see Figure 2). The value of this component is given by (see Proposition 35 in [17])

$$N(UZ^T) = (I - UU^T)\mathcal{L}(t, UZ^T)(I - Z(Z^TZ)^{-1}Z^T). \tag{45}$$

Since the singular value $\sigma_{r_\Psi+1}(\Psi^n + \Delta t \overline{L(t^n, \Psi^n)})$ after a step $\Delta t$ is of magnitude $\sigma_1(N(\Psi^n))\Delta t$ (see [27]), this first and other singular values of $N(UZ^T)$ are related to the speed at which the solution exits the rank-$r_\Psi$ matrix manifold $\mathscr{M}$. Thus, a quantitative criterion that can track the rank of the true original solution is

$$\sigma_1(N(U^n(Z^n)^T))\Delta t > \overline{\sigma}. \tag{46}$$

A common value $\sigma$ can be used for the threshold $\sigma = \overline{\sigma} = \underline{\sigma}$ to detect when the rank of the DO subspace must be decreased/increased; hence the setting of this single $\sigma$ provides the desired lower bound for the smallest singular value of the covariance matrix $Z$. Singular vectors of $N(U^n(Z^n)^T)$ contain the new dominant directions. They can be combined with a gradient descent similar to (43) to compute the rank-$r_\Psi'$ (instead of $r_\Psi$) truncated SVD of $\Psi^{n+1} = \Psi^n + \Delta t \overline{L(t^n, \Psi^n)}$, while preserving the smooth evolution of the first $r_\Psi$ modes and coefficients (in contrast with the direct use of the algebraic Algorithm 3.1a). The procedure is summarized in Algorithm 3.2.

**3.5. Preserving the Orthonormality of the Mode Matrix $U$.** As highlighted in [80], an issue with time discretization, e.g., (36) or (43), is that, in general, the $l$-by-$r_\Psi$ matrix $U^{n+1} \in \mathcal{M}_{l,r_\Psi}$ obtained after a discrete time step does not exactly satisfy the orthogonality constraint $U^{n+1^T}U^{n+1} = I$. A numerical procedure must therefore be used to reduce the truncation errors committed by the discretization, even though the true trajectory $U(t)Z^T(t)$ on $\mathscr{M}$ and the DO equations (21) ensure and assume $U^TU = I$ at all instants. This procedure must be accurate, as numerical orthonormalization may also introduce round-off errors that can lead to significant error over large integration times. For example, standard and modified Gram–Schmidt

---

**Algorithm 3.2** Augmenting the rank of the DO solution

---

1: Compute $\mathbf{\Psi}^{n+1} = U^n (Z^n)^T + \Delta L_U^n (L_Z^n)^T$ with $L_U \in \mathcal{M}_{l,r_{\overline{L}}}, L_Z^n \in \mathcal{M}_{m,r_{\overline{L}}}$ as in (42).

2: Compute the normal component (of rank at most $r_{\overline{L}}$) at $t^n$:

$$N(U^n (Z^n)^T) = [(I - U^n (U^n)^T) L_U^n][(L_Z^n)^T (I - Z^n ((Z^n)^T Z^n)^{-1} (Z^n)^T)].$$

3: Compute the rank-$r_{\Psi}' - r_{\Psi} < r_{\overline{L}}$ truncated SVD of $N(U^n (Z^n)^T)$, i.e., $N_U^n (N_Z^n)^T$, using Algorithm 3.1a.

4: Use the gradient descent (43) starting from the initialization values $U_0 = [U^n N_U^n]$ and $Z_0 = [Z^n N_Z^n]$, to find the truncated SVD of rank $r_{\Psi}' > r_{\Psi}$ of $\mathbf{\Psi}^{n+1}$, i.e., $U^{n+1} (Z^{n+1})^T$.

---

orthonormalization presents numerical instabilities when $UZ^T$ becomes close to being rank deficient (see [76]). For this reason, [79, 80] used the following procedure: compute the eigendecomposition of the Gram matrix $K = U^T U$,

$$(47) \qquad\qquad\qquad PKP^T = \Sigma.$$

Then rotate and scale modes and coefficients accordingly by setting

$$(48) \qquad\qquad\qquad \begin{cases} U \leftarrow UP\Sigma^{-1/2}, \\ Z \leftarrow ZP\Sigma^{1/2}. \end{cases}$$

The eigenvalue problem (47) can be solved using Householder factorization, which is known to be numerically stable in comparison with Gram–Schmidt orthonormalization [76]. An issue is that this procedure may introduce permutations or sign changes, leading to artificial discontinuities in the time evolution of the mode and coefficient matrices $U$ and $Z$. Figure 4 illustrates the problem by plotting the typical evolution of a coefficient of the matrix $Z$ with this orthonormalization procedure. Even though sign checks alleviate the problem [80], they are a burden. Hence, to reinforce orthogonality between time steps and provide smooth evolutions for both $U$ and $Z$ (21), one can employ a gradient flow, as was done in the DO time-stepping (43). Reorthonormalization is then performed by finding an invertible matrix $A \in \mathcal{M}_{r_{\Psi}, r_{\Psi}}$ such that $(UA)^T (UA) = A^T K A = I$ and by setting $U \leftarrow UA$ and $Z \leftarrow ZA^{-T}$. Such a matrix
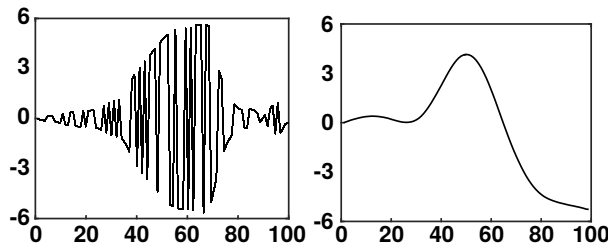


**Fig. 4** *Evolution of a coefficient of the matrix $Z^n$ obtained by the time integration of (21) as a function of the iteration number. On the left, reorthonormalization of the matrix $U^n$ is performed by solving the eigenvalue problem (48), while on the right, the gradient flow (49) was used. Eigenvalue decompositions introduce sign flips and permutations that result in artificial discontinuities in the individual matrices $U^n$ and $Z^n$ if dealt with algebraically [80].*

$A$ is actually the minimizer over $\mathcal{M}_{r_\Psi, r_\Psi}$ of the functional

$$G(A) = \frac{1}{4} ||A^T K A - I||^2.$$

Therefore, one can find a reorthonormalization matrix $A$ close to the identity by solving the gradient flow

(49)
$$\frac{\mathrm{d}A}{\mathrm{d}s} = -\frac{\mathrm{d}G}{\mathrm{d}A} = -KA(A^T K A - I)$$

with initial value $A(0) = I$. The inverse $A^{-1}$ of $A$ can be simultaneously tracked by solving the ODE

$$\frac{\mathrm{d}A^{-1}}{\mathrm{d}s} = -A^{-1} \frac{\mathrm{d}A}{\mathrm{d}s} A^{-1}.$$

The resulting numerical procedure is summarized in Algorithm 3.3. Typically, one expects $A = I + O(||U^T U - I||)$ and hence both corrections $UA \simeq U$ and $ZA^{-T} \simeq Z$ will have an order of magnitude identical to the initial error, ensuring the smooth evolution of $U$ and $Z$. Figure 4 shows the time evolution of a coefficient of the matrix $Z$ using this method. Only a few Euler steps are necessary to obtain convergence, which makes the method efficient. The matrix $A \simeq I$ is well conditioned and the Algorithm 3.3 has small round-off errors.

---

**Algorithm 3.3** Reorthonormalization procedure of $UZ^T \in \mathcal{M}$ with $U^T U \simeq I$
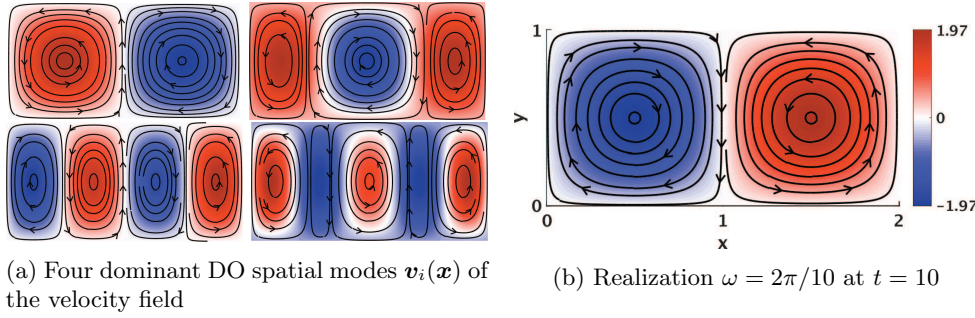
---

1: Define a tolerance parameter $\epsilon$ and a time step $\mu$ (typically $\mu \simeq 1$).
2: $K \leftarrow U^T U$
3: $A \leftarrow I,\ A^{-1} \leftarrow I$
4: **while** $||A_k^T K A_k - I||^2 > \epsilon$ **do**
5: $\quad \mathrm{d}A_k \leftarrow -KA_k(A_k^T K A_k - I)$
6: $\quad A_{k+1} \leftarrow A_k + \mu \mathrm{d}A_k$
7: $\quad A_{k+1}^{-1} \leftarrow A_k^{-1} - \mu A_k^{-1}(\mathrm{d}A_k)A_k^{-1}$
8: $\quad k \leftarrow k + 1$
9: **end while**
10: $U \leftarrow UA_k$ and $Z \leftarrow ZA_k^{-T}$

---

## 4. Numerical Results.

**4.1. Stochastic Double-Gyre Flow.** The double gyre is the classic 2D benchmark flow for the study of Lagrangian coherence of particle motions [67, 44, 25]. The idealized flow consists of two vortices oscillating horizontally. Currently, the above new schemes are utilized to analyze how the Lagrangian motion of particles is affected by the oscillation angular frequency $\omega$. Hence, a range of initial $\omega$ values is considered and $\omega$ is modeled as an unknown random parameter. The classic analytical deterministic flow [67] then becomes stochastic (Figure 5):

$$\boldsymbol{v}(t, \boldsymbol{x}; \omega) = (-\partial_y \phi, \partial_x \phi) \quad \text{with } \phi(\boldsymbol{x}, t; \omega) = A \sin[\pi f(x, t; \omega)] \sin(\pi y),$$

where $f(x, t; \omega) = \epsilon \sin(\omega t)x^2 + (1 - 2\epsilon \sin(\omega t))x$, $\boldsymbol{x} = (x, y)$, and $\omega$ is initially random. The fixed parameter values here are $A = 0.1$ and $\epsilon = 0.1$. The goal is to provide solutions to the SPDE (6), up to time $t = 10$ and for $\omega$ uniformly distributed within $[\pi/10, 8\pi/10]$.

(a) Four dominant DO spatial modes $\boldsymbol{v}_i(\boldsymbol{x})$ of the velocity field

(b) Realization $\omega = 2\pi/10$ at $t = 10$

**Fig. 5** *Stochastic double-gyre flow with an initially random oscillation angular frequency. Streamlines are overlaid on the colored intensity of the vorticity.*

For the DO computations, the spatial domain $[0, 2] \times [0, 1]$ is discretized using a $257 \times 129$ grid with $l_{bc} = 2 \times 768$ boundary nodes and the stochastic domain $[\pi/10, 8\pi/10]$ with $m = 10{,}000$ realizations $\omega_\alpha$ uniformly distributed according to

$$\omega_\alpha = \frac{\pi}{10} + \left( \frac{\alpha - 1}{m - 1} \right) \frac{7\pi}{10}, \ 1 \le \alpha \le m.$$

Hence, in this example, $l = 2 \times (257 \times 129 - 768) = 64{,}770$. The threshold used for increasing the stochastic dimensionality (eq. (46)) is set to $\sigma = 10^{-2}$. The retraction used in the DO time-marching is that of subsection 3.3.3, computed with the gradient descent of Algorithm 3.1b.

The stochastic velocity is decomposed into four time-independent modes $\boldsymbol{v}_i(\boldsymbol{x})$ (Figure 5), and coefficients $\beta_i(t; \omega) = \langle \boldsymbol{v}_i(\boldsymbol{x}), \boldsymbol{v}(t, \boldsymbol{x}; \omega) \rangle$ are obtained by orthogonal projection. They force the SPDE (6). The initial value $\boldsymbol{\psi}(0, \boldsymbol{x}; \omega) = \boldsymbol{x}$ of the flow-map solution is shown in Figure 6.



(a) $x$ coordinate

(b) $y$ coordinate
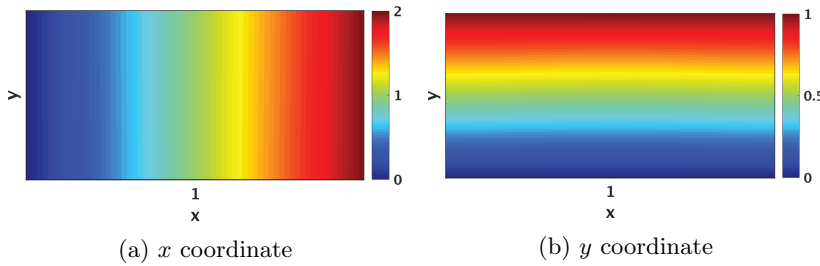
**Fig. 6** *Initial value $\boldsymbol{\psi}(0, \boldsymbol{x}; \omega) = \boldsymbol{x}$ of the advection equation (6).*

To first validate the fully linear sixth-order-central, RK3, Shapiro filter scheme selected in subsection 3.1, the PDE (6) is first solved directly backward in time (forward flow-map) for a fixed value of $\omega = 2\pi/10$ until $t = 10$ and contrasted with the popular fifth-order WENO scheme combined with the TVDRK3 time-stepping [54]. The two solutions and their differences are shown in Figure 7. As expected from the 1D example (Figure 3), the fully linear scheme induces very small numerical errors near shocks, by either smearing or overshooting small details. Indeed, the two flow-map solutions are very comparable, which demonstrates the broad applicability of this fully linear scheme for advection (e.g., they are used in ocean modeling [34, 23, 22]). The scheme is therefore to solve the DO equations (21), as discussed in section 3.

(a) $x$ coordinate                    (b) $y$ coordinate
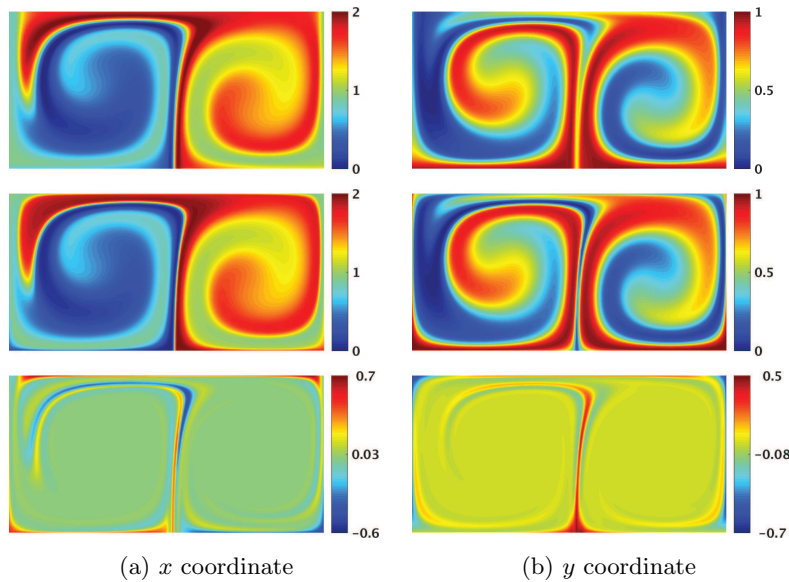
**Fig. 7**  *Comparison between linear sixth-order-central, RK3, Shapiro filter (top) and nonlinear WENO–TVDRK3 (middle) advection schemes for the deterministic solutions of (6) run backward in time (without model order reduction), for the realization $\omega = 2\pi/10$, the difference being plotted below (bottom).*

The stochastic (forward) flow-map DO simulation (21) is run with $r_\Psi = 20$ modes. For numerical stability, the eighth-order Shapiro filter $\mathcal{F}^{(8)}$ (eq. (30)) is applied at every time step instead of every 10 as in Figure 7. The first four DO modes obtained from the truncated SVD at $t = 10$ are displayed in Figure 8. This figure illustrates the ability of the DO solution to capture dominant modes that are spatially localized and that include shocks (hence are far from being Fourier modes) and multimodal distributions of the coefficients that are far from being Gaussian.

Three deterministic flow-map realizations, obtained by directly solving the transport PDE (6) for $\omega \in \{2\pi/10, 5\pi/10, 8\pi/10\}$, are compared to the corresponding DO solutions in Figure 9. The figure shows excellent agreement, which is a key result. The approximation of the solution by 20 modes incurs the loss of some sharp features, but the agreement between MC and DO realizations shows that the stochasticity of the flow-map is well captured by the low-dimensional time-dependent DO basis. The CPU time (with MATLAB) required by the DO simulation for $m = 10{,}000$ realizations is $\text{CPU}_{\text{DO}} = 3{,}530$. That of each MC realization requires $\text{CPU}_{\text{MC}} = 135$. The observed computational speed-up is therefore $\frac{\text{CPU}_{\text{MC}} \times m}{\text{CPU}_{\text{DO}}} \simeq 382$. This is consistent with the prediction given by the ratio $\frac{lm}{(l+m)r_\Psi - r_\Psi^2} \simeq 433$ between the dimension of the ambient space and that of the manifold $\mathcal{M}$.

The mean and the standard deviation fields of the stochastic flow-map are computed efficiently in a straightforward manner from the DO decomposition and are displayed in Figure 10. These results highlight the mean behavior of the flow-map (panels a and b) and the regions characterized by an increased level of uncertainty (panel c). They confirm that neither the mean fields nor the standard deviation field are symmetric with respect to the $y$-axis at $t = 10$ because $\omega$ is uniformly distributed within $[\pi/10, 8\pi/10]$. At that time, positions with the largest flow-map uncertainties

(a) $x$ coordinate           (b) $y$ coordinate

(c) Coefficient distributions
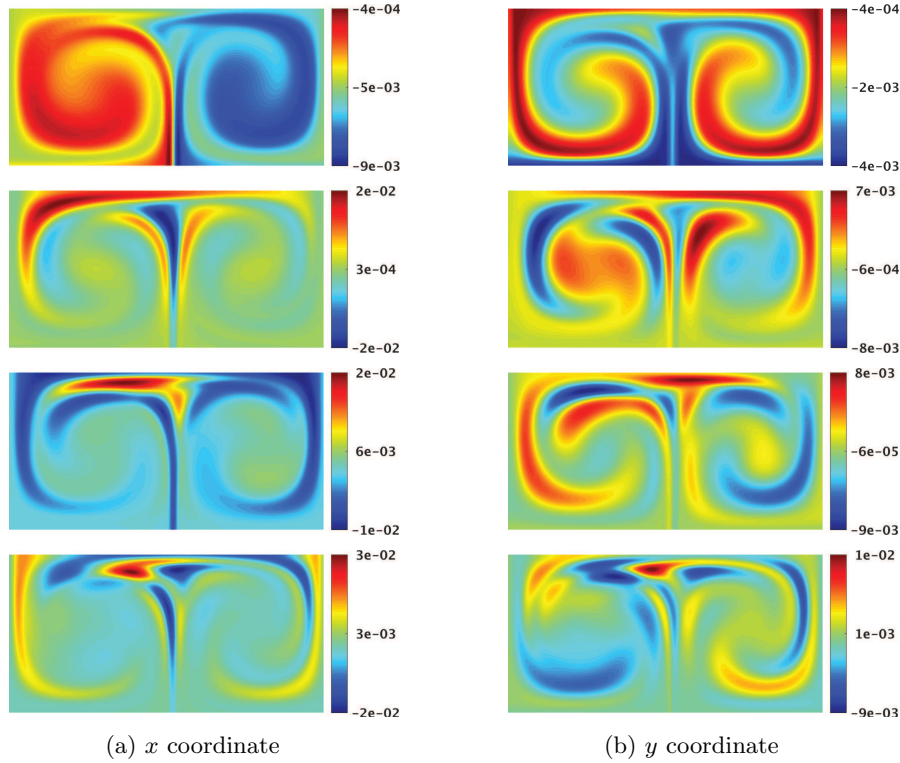
**Fig. 8** *Dominant first four SVD modes $\boldsymbol{\psi}_i$ (from top to bottom) and histogram of the corresponding distributions of the coefficients $\zeta_i$ (from left to right) of the forward flow-map DO solution $\boldsymbol{\psi}$ for the double-gyre example at $t = 10$.*

are located at low $y$ values, near the two extreme $x$ values. These results critically illustrate the applicability of the new DO schemes for the study of Lagrangian transports under a stochastic velocity field.
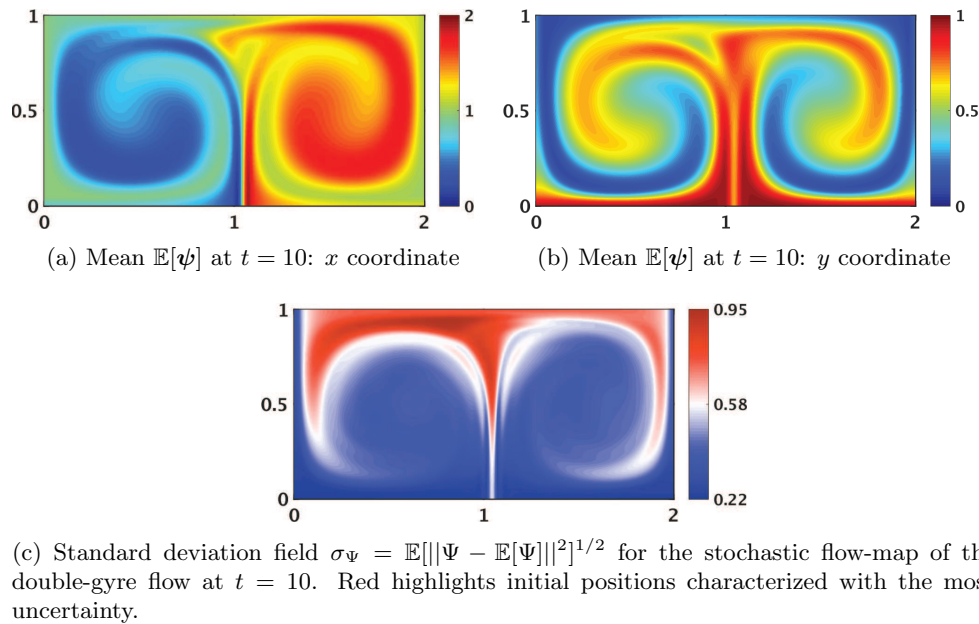
**4.2. Stochastic Flow Past a Cylinder.** The stochastic flow past a cylinder is now considered as a more realistic uncertain flow field. The nondimensional flow is set on a domain of size 16-by-6 and discretized on a $240 \times 90$ grid with $l_{bc} = 2 \times 176$ boundary or obstacle nodes. The Reynolds number is Re = 100. The cylinder is a disc of center $(x_c, y_c) = (4.5, 3)$ and of radius $R = 0.5$. The flow enters at the left side of the domain with a velocity $\boldsymbol{v} = (1, 0)$. Neumann BCs are considered at the top and bottom walls, while the second normal derivative is set to $\partial^2 \boldsymbol{v}/\partial n^2 = 0$ at the outlet on the right. A random perturbation is used to initiate a stochastic flow $\boldsymbol{v}(t, \boldsymbol{x}; \omega)$ with periodic regime.

(a) $\omega = 2\pi/10$
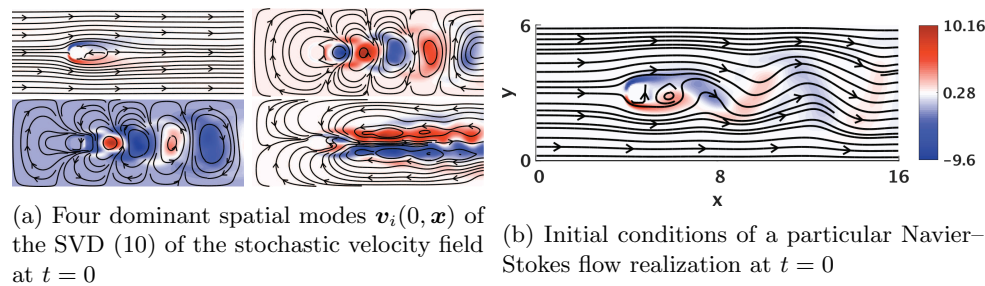


(b) $\omega = 5\pi/10$



(c) $\omega = 8\pi/10$
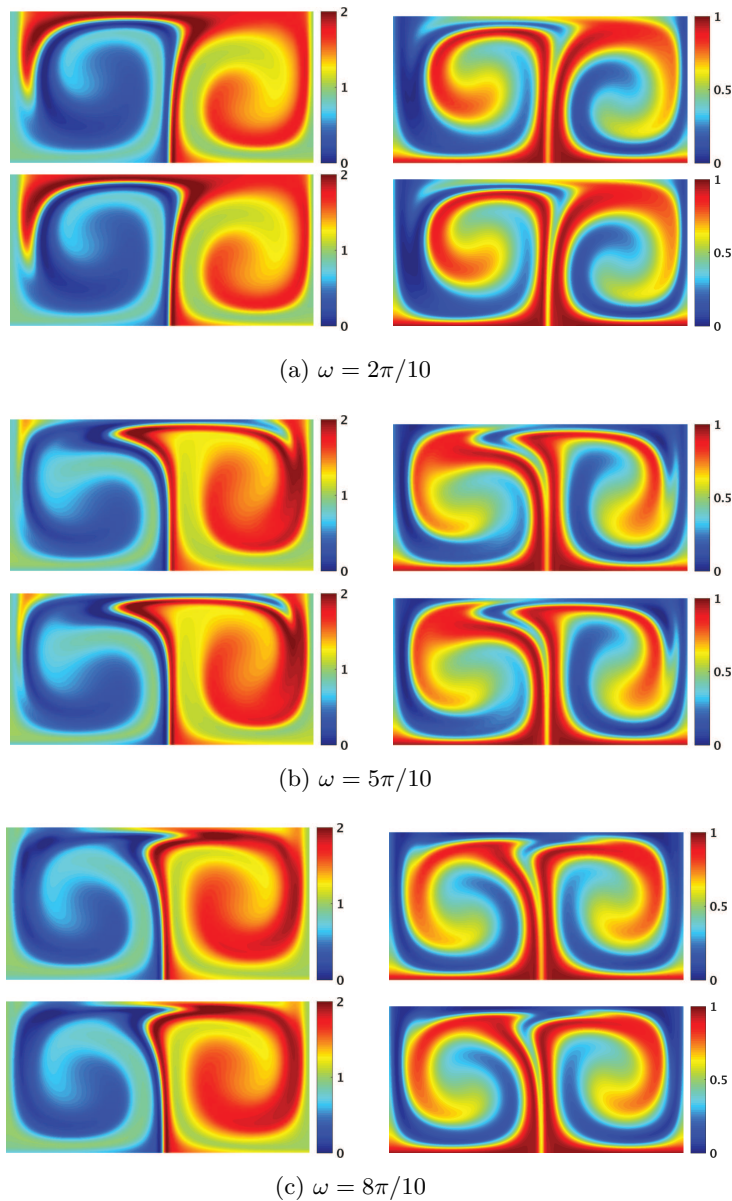
**Fig. 9** *Evaluation of the DO results (*above*) by comparison with direct MC simulations (*below*) for three double-gyre frequencies $\omega$ and for both $x$ (*left column*) and $y$ (*right column*) coordinates for the forward flow-map. The color scale is identical to that of Figure 6.*

For the DO flow-map computations (6), $m = 10{,}000$ realizations of the flow are obtained from a DO simulation of the Navier–Stokes equations with the numerical schemes described in [80]. The time window considered is $[0, 10]$, and the initial time, $t = 0$, is started once the periodic regime is established. Hence, in this example, $l = 2(240 \times 90 - 176) = 42{,}848$. The threshold for increasing the stochastic dimensionality (eq. (46)) is again set to $\sigma = 10^{-2}$ and the retraction is that of subsection 3.3.3 computed with Algorithm 3.1b.

(a) Mean $\mathbb{E}[\boldsymbol{\psi}]$ at $t = 10$: $x$ coordinate



(b) Mean $\mathbb{E}[\boldsymbol{\psi}]$ at $t = 10$: $y$ coordinate



(c) Standard deviation field $\sigma_\Psi = \mathbb{E}[||\Psi - \mathbb{E}[\Psi]||^2]^{1/2}$ for the stochastic flow-map of the double-gyre flow at $t = 10$. Red highlights initial positions characterized with the most uncertainty.

**Fig. 10** *Statistical quantities of the stochastic forward flow-map for the double-gyre flow at $t = 10$, as computed from the stochastic DO simulation. For (a) and (b), the color scale is identical to that of Figure 6.*



(a) Four dominant spatial modes $\boldsymbol{v}_i(0, \boldsymbol{x})$ of the SVD (10) of the stochastic velocity field at $t = 0$



(b) Initial conditions of a particular Navier–Stokes flow realization at $t = 0$

**Fig. 11** *Stochastic flow past a cylinder: stochastic DO velocity initialization. Streamlines are overlaid on the colored intensity of the vorticity.*

The stochastic DO velocity initialization is illustrated in Figure 11. The first four dominant modes of this flow along with one particular realization are shown. The stochastic (forward) flow-map is computed analogously to the previous example with $r_\Psi = 20$ modes and the Shapiro filter $\mathcal{F}^{(8)}$ being applied at every time step. Figure 12 displays the values of the first four dominant modes and the corresponding coefficient distributions of the SVD (eq. (22)) of the flow-map solution at time $t = 10$.

Three particular deterministic forward flow-map realizations, $\omega_1$, $\omega_2$, and $\omega_3$, are evaluated directly and compared to the corresponding DO solution in Figure 13. Again, excellent agreement is observed between the MC realizations and the DO reconstructed solutions.

Similarly as above, the mean and standard deviation fields of the resulting Lagrangian motion are shown in Figure 14. Since particles may exit the domain, the

(a) $x$ coordinate

(b) $y$ coordinate

(c) Coefficient distributions
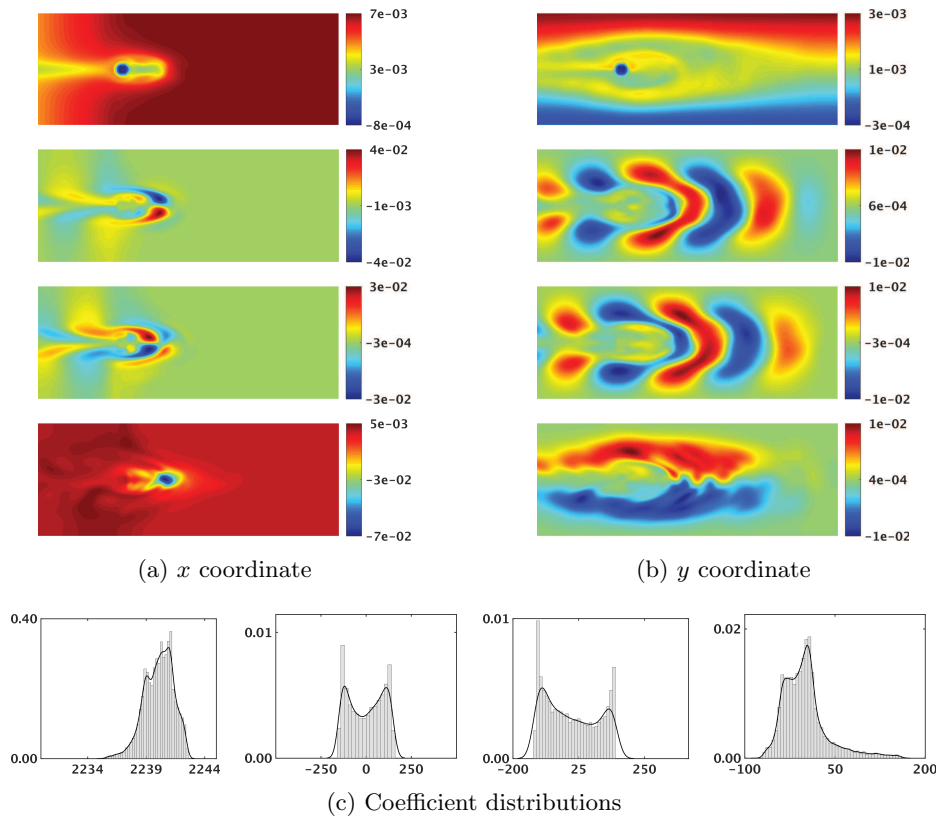
**Fig. 12** *Dominant first four SVD* (22) *modes* $\boldsymbol{\psi}_i$ *and histogram of the corresponding distributions of the coefficients* $\zeta_i$ *of the forward flow-map DO solution* $\boldsymbol{\psi}$ *for the flow past a cylinder example at* $t = 10$.

value of $\boldsymbol{\psi}(10, \boldsymbol{x}; \omega)$ is the final position occupied by a particle initially located at $\boldsymbol{x}$ at time $t = 0$ if this particle does not leave the domain, or the position of where the particle left the domain otherwise. Recall here that $l = 42{,}848$ and $m = 10{,}000$. The observed CPU times required for the forward flow-map DO simulation and one MC realization are, respectively, $\text{CPU}_{\text{DO}} = 940$ and $\text{CPU}_{\text{MC}} \simeq 32$. This yields an effective computational speed-up of $\frac{\text{CPU}_{\text{MC}} \times m}{\text{CPU}_{\text{DO}}} \simeq 340$, still consistent with the prediction $\frac{lm}{(l+m)r_\Psi - r_\Psi{}^2} \simeq 405$.
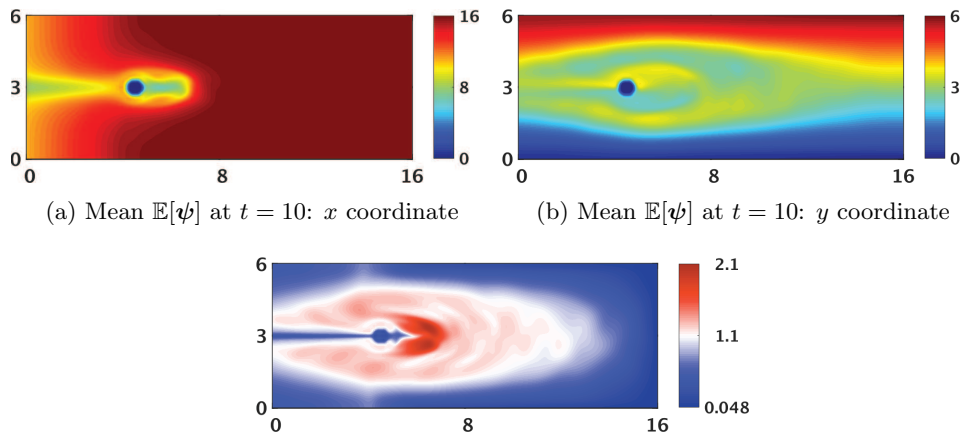
**5. Conclusion.** The dynamically orthogonal (DO) decomposition and its geometric interpretations were utilized to obtain systematic optimal reduced order discrete equations and novel numerical schemes for stochastic advection and Lagrangian transport. The implementation of the DO methodology was thoroughly reviewed and improved by exploiting its relation to the dynamically truncated SVD. Its broad applicability to treat advection was illustrated, offering a novel and efficient method of computing a large number of realizations of the flow-map of an ODE with stochastic velocity. Fully linear, high-order stabilized advection schemes were shown to provide deterministic-stochastic consistency and compatible reduced-order schemes for dynamic linear model order reduction. A set of schemes was provided and utilized to account for the curvature of the fixed-rank manifold, to dynamically evolve the rank of

(a) $\omega_1$

(b) $\omega_2$

(c) $\omega_3$
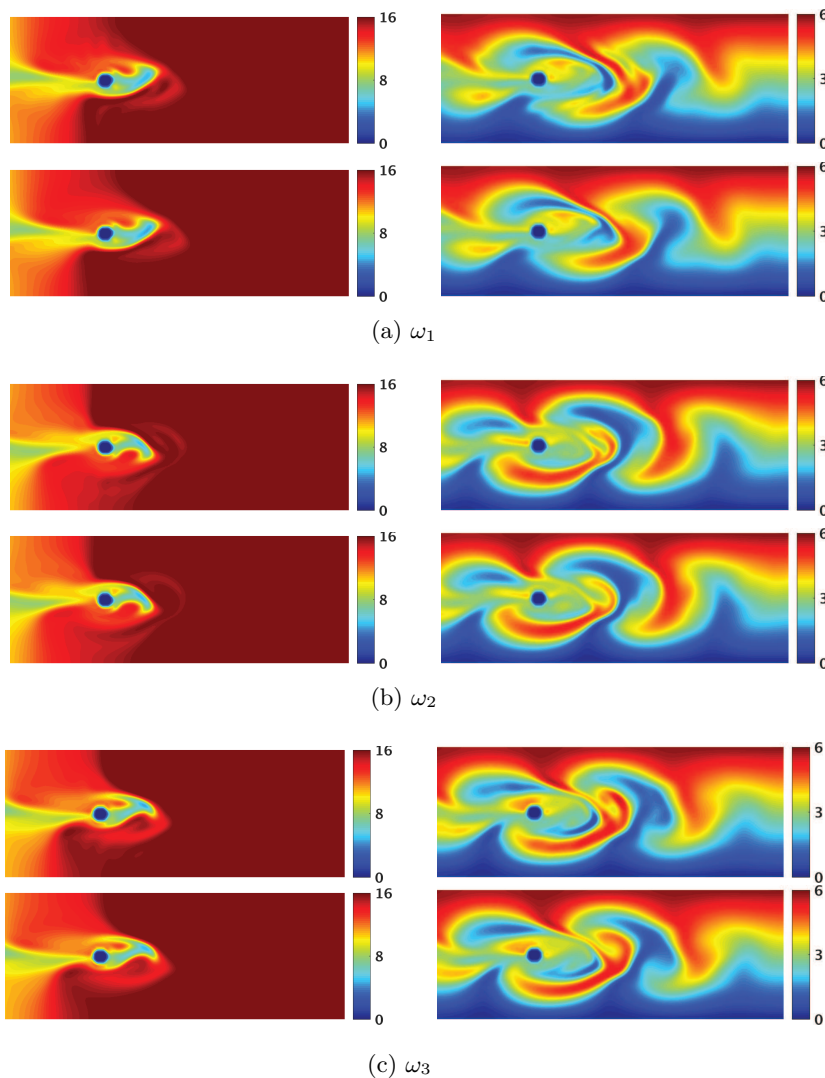
**Fig. 13** *Evaluation of the DO results (*above*) by comparison with direct MC simulations (*below*) for three forward flow-map realizations for $\omega_1$, $\omega_2$, $\omega_3$ and for both $x$ (*left column*) and $y$ (*right column*) coordinates. The color scale is identical to that of Figure 6.*

the reduced solution, and to ensure the smooth evolution of the orthonormal modes. The effectiveness of the novel time-marching DO equations and numerical schemes for uncertain Lagrangian transport was demonstrated on the analytic stochastic double-gyre flow, a benchmark for Lagrangian coherent structures studies, and on stochastic velocity data obtained from a numerical simulation of the flow past a cylinder, a sensitive test for advection schemes.

(a) Mean $\mathbb{E}[\boldsymbol{\psi}]$ at $t = 10$: $x$ coordinate



(b) Mean $\mathbb{E}[\boldsymbol{\psi}]$ at $t = 10$: $y$ coordinate



(c) Standard deviation field $\sigma_\Psi = \mathbb{E}[||\Psi - \mathbb{E}[\Psi]||^2]^{1/2}$ for the stochastic DO forward flow-map of the flow past a cylinder at $t = 10$. Red highlights initial positions characterized with the most uncertainty.

---

**Fig. 14** *Statistical quantities of the stochastic DO forward flow-map corresponding to the stochastic flow past a cylinder at $t = 10$, itself computed from a stochastic DO Navier–Stokes simulation. For (a) and (b), the color scale is identical to that of Figure 6.*

REFERENCES

[1] P.-A. ABSIL AND J. MALICK, *Projection-like retractions on matrix manifolds*, SIAM J. Optim., 22 (2012), pp. 135–158, https://doi.org/10.1137/100802529. (Cited on pp. 604, 608, 609, 610)

[2] L. AMBROSIO, *Transport equation and Cauchy problem for non-smooth vector fields*, in Calculus of Variations and Nonlinear Partial Differential Equations, Springer, 2008, pp. 1–41. (Cited on pp. 596, 597)

[3] A. BENNETT, *Lagrangian Fluid Dynamics*, Cambridge University Press, 2006. (Cited on p. 596)

[4] F. BOYER, *Trace theorems and spatial continuity properties for the solutions of the transport equation*, Differential Integral Equations, 18 (2005), pp. 891–934. (Cited on pp. 597, 600)

[5] R. W. BROCKETT, *Dynamical systems that sort lists, diagonalize matrices and solve linear programming problems*, in Proceedings of the 27th IEEE Conference on Decision and Control, IEEE, 1988, pp. 799–803. (Cited on p. 598)

[6] G.-H. COTTET AND P. D. KOUMOUTSAKOS, *Vortex Methods: Theory and Practice*, Cambridge University Press, 2000. (Cited on p. 597)

[7] D. N. DAESCU AND I. M. NAVON, *Efficiency of a POD-based reduced second-order adjoint model in 4D-var data assimilation*, Internat. J. Numer. Methods Fluids, 53 (2007), pp. 985–1004. (Cited on p. 598)

[8] J. DEHAENE, *Continuous-Time Matrix Algorithms Systolic Algorithms and Adaptive Neural Networks*, Ph.D. thesis, Katholieke Universiteit Leuven, 1995. (Cited on p. 598)

[9] R. J. DIPERNA AND P.-L. LIONS, *Ordinary differential equations, transport theory and Sobolev spaces*, Invent. Math., 98 (1989), pp. 511–547. (Cited on pp. 596, 597)

[10] A. DOOSTAN, R. G. GHANEM, AND J. RED-HORSE, *Stochastic model reduction for chaos representations*, Comput. Methods Appl. Mech. Engrg., 196 (2007), pp. 3951–3966. (Cited on p. 598)

[11] D. R. DURRAN, *The third-order Adams-Bashforth method: An attractive alternative to leapfrog time differencing*, Monthly Weather Rev., 119 (1991), pp. 702–720. (Cited on p. 606)

[12] A. EDELMAN, T. A. ARIAS, AND S. T. SMITH, *The geometry of algorithms with orthogonality constraints*, SIAM J. Matrix Anal. Appl., 20 (1998), pp. 303–353, https://doi.org/10.1137/S0895479895290954. (Cited on p. 598)

[13] M. A. EL-BELTAGY, M. I. WAFA, AND O. H. GALAL, *Upwind finite-volume solution of stochastic Burgers' equation*, Appl. Math., 03 (2012), pp. 1818–1825. (Cited on p. 598)

[14] B. ENGQUIST, P. LÖTSTEDT, AND B. SJÖGREEN, *Nonlinear filters for efficient shock computation*, Math. Comp., 52 (1989), pp. 509–537. (Cited on p. 606)

[15] R. ERRICO, *What is an adjoint model?*, Bull. Amer. Meteorol. Soc., 78 (1997), pp. 2577–2592. (Cited on p. 612)

[16] B. FARRELL AND P. IOANNOU, *Generalized stability theory part* I: *Autonomous operators*, J. Atmos. Sci., 53 (1996), pp. 2025–2040. (Cited on p. 612)

[17] F. FEPPON AND P. F. J. LERMUSIAUX, *A geometric approach to dynamical model-order reduction*, SIAM J. Matrix Anal. Appl., 39 (2018), pp. 510–538, https://doi.org/10.1137/16M1095202. (Cited on pp. 598, 599, 601, 602, 603, 604, 608, 609, 610, 611, 612)

[18] S. K. GODUNOV, *A difference method for numerical calculation of discontinuous solutions of the equations of hydrodynamics*, Mat. Sb. (N.S.), 89 (1959), pp. 271–306. (Cited on p. 606)

[19] V. M. GOLOVIZNIN, V. N. SEMENOV, I. A. KOROTKIN, AND S. A. KARABASOV, *A novel computational method for modelling stochastic advection in heterogeneous media*, Transp. Porous Media, 66 (2007), pp. 439–456. (Cited on pp. 597, 598)

[20] A. GRIFFA, A. KIRWAN, JR., A. J. MARIANO, T. ÖZGÖKMEN, AND H. T. ROSSBY, *Lagrangian Analysis and Prediction of Coastal and Ocean Dynamics*, Cambridge University Press, 2007. (Cited on p. 596)

[21] A. GUPTA AND P. F. J. LERMUSIAUX, *Boundary Conditions for Stochastic DO Equations*, MSEAS Report, Department of Mechanical Engineering, MIT, Cambridge, MA, 2016. (Cited on pp. 601, 607, 608)

[22] P. J. HALEY, JR., A. AGARWAL, AND P. F. J. LERMUSIAUX, *Optimizing velocities and transports for complex coastal regions and archipelagos*, Ocean Modeling, 89 (2015), pp. 1–28. (Cited on p. 615)

[23] P. J. HALEY, JR., AND P. F. J. LERMUSIAUX, *Multiscale two-way embedding schemes for free-surface primitive equations in the "Multidisciplinary Simulation, Estimation and Assimilation System,"* Ocean Dynam., 60 (2010), pp. 1497–1537. (Cited on p. 615)

[24] P. J. HALEY, JR., AND P. F. J. LERMUSIAUX, *Limiters for Shapiro Filtering with Primitive-Equation Ocean Models*, MSEAS Report, Department of Mechanical Engineering, MIT, Cambridge, MA, 2016. (Cited on p. 606)

[25] G. HALLER, *Lagrangian coherent structures*, Annu. Rev. Fluid Mech., 47 (2015), pp. 137–162. (Cited on p. 614)

[26] P. HOLMES, J. L. LUMLEY, AND G. BERKOOZ, *Turbulence, Coherent Structures, Dynamical Systems and Symmetry*, Cambridge University Press, 1998. (Cited on pp. 596, 598)

[27] R. A. HORN AND C. R. JOHNSON, *Matrix Analysis*, Cambridge University Press, 2009. (Cited on pp. 603, 612)

[28] M. JARDAK, C.-H. SU, AND G. E. KARNIADAKIS, *Spectral polynomial chaos solutions of the stochastic advection equation*, J. Sci. Comput., 17 (2002), pp. 319–338. (Cited on p. 598)

[29] E. KALNAY, *Atmospheric Modeling, Data Assimilation and Predictability*, Cambridge University Press, 2002. (Cited on p. 612)

[30] O. KOCH AND C. LUBICH, *Dynamical low-rank approximation*, SIAM J. Matrix Anal. Appl., 29 (2007), pp. 434–454, https://doi.org/10.1137/050639703. (Cited on pp. 598, 599, 603, 604)

[31] J. N. KUTZ, S. L. BRUNTON, B. W. BRUNTON, AND J. L. PROCTOR, *Dynamic Mode Decomposition: Data-Driven Modeling of Complex Systems*, SIAM, 2016, https://doi.org/10.1137/1.9781611974508. (Cited on p. 598)

[32] F. LAFON AND S. OSHER, *High order filtering methods for approximating hyperbolic systems of conservation laws*, J. Comput. Phys., 96 (1991), pp. 110–142. (Cited on p. 606)

[33] F. LEKIEN, C. COULLIETTE, A. J. MARIANO, E. H. RYAN, L. K. SHAY, G. HALLER, AND J. MARSDEN, *Pollution release tied to invariant manifolds: A case study for the coast of Florida*, Phys. D, 210 (2005), pp. 1–20. (Cited on p. 597)

[34] P. F. LERMUSIAUX, *Error Subspace Data Assimilation Methods for Ocean Field Estimation: Theory, Validation and Applications*, Harvard University, 1997. (Cited on pp. 598, 599, 606, 615)

[35] P. F. J. LERMUSIAUX, *Data assimilation via error subspace statistical estimation, part* II: *Mid-Atlantic bight shelfbreak front simulations, and ESSE validation*, Monthly Weather Rev., 127 (1999), pp. 1408–1432. (Cited on p. 612)

[36] P. F. J. LERMUSIAUX, *Estimation and study of mesoscale variability in the Strait of Sicily*, Dynam. Atmospheres Oceans, 29 (1999), pp. 255–303. (Cited on p. 598)

[37] P. F. J. LERMUSIAUX, *Evolving the subspace of the three-dimensional multiscale ocean variability: Massachusetts Bay*, J. Marine Syst., 29 (2001), pp. 385–422. (Cited on p. 598)

[38] P. F. J. LERMUSIAUX, *On the mapping of multivariate geophysical fields: Sensitivities to size, scales, and dynamics*, J. Atmospheric Oceanic Technol., 19 (2002), pp. 1602–1637. (Cited on p. 603)

[39] P. F. J. LERMUSIAUX, *Uncertainty estimation and prediction for interdisciplinary ocean dynamics*, J. Comput. Phys., 217 (2006), pp. 176–199. (Cited on p. 597)

[40] P. F. J. LERMUSIAUX, D. G. M. ANDERSON, AND C. J. LOZANO, *On the mapping of multivariate geophysical fields: Error and variability subspace estimates*, Quart. J. Roy. Meteorological Soc., 126 (2000), pp. 1387–1429. (Cited on p. 603)

[41] P. F. J. LERMUSIAUX, C.-S. CHIU, G. G. GAWARKIEWICZ, P. ABBOT, A. R. ROBINSON, R. N. MILLER, P. J. HALEY, JR., W. G. LESLIE, S. J. MAJUMDAR, A. PANG, AND F. LEKIEN, *Quantifying uncertainties in ocean predictions*, Oceanography, 19 (2006), pp. 92–105. (Cited on p. 597)

[42] P. F. J. LERMUSIAUX AND F. LEKIEN, *Dynamics and Lagrangian coherent structures in the ocean and their uncertainty*, in Dynamical System Methods in Fluid Dynamics, Oberwolfach Workshop, J. E. Marsden and J. Scheurle, eds., Mathematisches Forschungsinstitut Oberwolfach, Germany, 2005, p. 2. (Cited on p. 597)

[43] P. F. J. LERMUSIAUX AND A. R. ROBINSON, *Data assimilation via error subspace statistical estimation, part* I: *Theory and schemes*, Monthly Weather Rev., 127 (1999), pp. 1385–1407. (Cited on p. 612)

[44] S. LEUNG, *An Eulerian approach for computing the finite time Lyapunov exponent*, J. Comput. Phys., 230 (2011), pp. 3500–3524. (Cited on pp. 597, 600, 614)

[45] S. LEUNG, *The backward phase flow method for the Eulerian finite time Lyapunov exponent computations*, Chaos, 23 (2013), 043132. (Cited on p. 597)

[46] M. LEUTBECHER AND T. PALMER, *Ensemble forecasting: Predicting weather, climate and extreme events*, J. Comput. Phys., 227 (2008), pp. 3515–3539. (Cited on p. 597)

[47] R. J. LEVEQUE, *Finite Volume Methods for Hyperbolic Problems*, Cambridge University Press, 2002. (Cited on p. 602)

[48] T. LOLLA, *Path Planning in Time Dependent Flows Using Level Set Methods*, master's thesis, Department of Mechanical Engineering, MIT, 2012. (Cited on p. 598)

[49] C. LUBICH AND I. V. OSELEDETS, *A projector-splitting integrator for dynamical low-rank approximation*, BIT, 54 (2014), pp. 171–188. (Cited on p. 599)

[50] B. MISHRA, G. MEYER, S. BONNABEL, AND R. SEPULCHRE, *Fixed-rank matrix factorizations and Riemannian low-rank optimization*, Comput. Statist., 29 (2014), pp. 591–621. (Cited on pp. 608, 609)

[51] A. MOORE AND R. KLEEMAN, *The singular vectors of a coupled ocean-atmosphere model of ENSO.* I: *Thermodynamics, energetics and error growth*, Quart. J. Roy. Meteorological Soc., 123 (2007), pp. 953–981. (Cited on p. 612)

[52] E. MUSHARBASH, F. NOBILE, AND T. ZHOU, *Error analysis of the dynamically orthogonal approximation of time dependent random PDEs*, SIAM J. Sci. Comput., 37 (2015), pp. A776–A810, https://doi.org/10.1137/140967787. (Cited on pp. 598, 599, 601, 604, 608)

[53] R. ONKEN, A. R. ROBINSON, P. F. J. LERMUSIAUX, P. J. HALEY, AND L. A. ANDERSON, *Data-driven simulations of synoptic circulation and transports in the Tunisia-Sardinia-Sicily region*, J. Geophys. Res. Oceans, 108 (2003). (Cited on p. 596)

[54] S. OSHER AND R. FEDKIW, *Level Set Methods and Dynamic Implicit Surfaces*, Appl. Math. Sci. 153, Springer Science & Business Media, 2006. (Cited on pp. 598, 602, 605, 615)

[55] S. OSHER AND C.-W. SHU, *High-order essentially nonoscillatory schemes for Hamilton–Jacobi equations*, SIAM J. Numer. Anal., 28 (1991), pp. 907–922, https://doi.org/10.1137/0728049. (Cited on p. 598)

[56] H. OSNES AND H. P. LANGTANGEN, *A study of some finite difference schemes for a unidirectional stochastic transport equation*, SIAM J. Sci. Comput., 19 (1998), pp. 799–812, https://doi.org/10.1137/S1064827593259108. (Cited on p. 598)

[57] T. N. PALMER, J. GELARO, J. BARKMEIJER, AND R. BUIZZA, *Singular vectors, metrics, and adaptive observations*, J. Atmos. Sci., 55 (1998), p. 633. (Cited on p. 612)

[58] A. PAPOULIS AND S. U. PILLAI, *Probability, Random Variables, and Stochastic Processes*, McGraw-Hill, 1985. (Cited on p. 600)

[59] J. QIU AND C.-W. SHU, *On the construction, comparison, and local characteristic decomposition for high-order central WENO schemes*, J. Comput. Phys., 183 (2002), pp. 187–209. (Cited on p. 606)

[60] C. W. ROWLEY, *Model reduction for fluids, using balanced proper orthogonal decomposition*, Internat. J. Bifur. Chaos, 15 (2005), pp. 997–1013. (Cited on p. 598)

[61] C. W. ROWLEY, I. MEZIĆ, S. BAGHERI, P. SCHLATTER, AND D. S. HENNINGSON, *Spectral analysis of nonlinear flows*, J. Fluid Mech., 641 (2009), pp. 115–127. (Cited on p. 598)

[62] R. M. SAMELSON AND S. WIGGINS, *Lagrangian Transport in Geophysical Jets and Waves: The Dynamical Systems Approach*, Interdiscip. Appl. Math. 31, Springer Science & Business Media, 2006. (Cited on p. 596)

[63] T. P. Sapsis and P. F. J. Lermusiaux, *Dynamically orthogonal field equations for continuous stochastic dynamical systems*, Phys. D, 238 (2009), pp. 2347–2360, https://doi.org/10.1016/j.physd.2009.09.017. (Cited on pp. 598, 599, 601, 605, 608)

[64] T. P. Sapsis and P. F. J. Lermusiaux, *Dynamical criteria for the evolution of the stochastic dimensionality in flows with uncertainty*, Phys. D, 241 (2012), pp. 60–76. (Cited on pp. 598, 611, 612)

[65] T. P. Sapsis, M. P. Ueckermann, and P. F. J. Lermusiaux, *Global analysis of Navier–Stokes and Boussinesq stochastic flows using dynamical orthogonality*, J. Fluid Mech., 734 (2013), pp. 83–113. (Cited on p. 598)

[66] P. J. Schmid, *Dynamic mode decomposition of numerical and experimental data*, J. Fluid Mech., 656 (2010), pp. 5–28. (Cited on p. 598)

[67] S. C. Shadden, F. Lekien, and J. E. Marsden, *Definition and properties of Lagrangian coherent structures from finite-time Lyapunov exponents in two-dimensional aperiodic flows*, Phys. D, 212 (2005), pp. 271–304. (Cited on p. 614)

[68] R. Shapiro, *Smoothing, filtering, and boundary effects*, Rev. Geophys., 8 (1970), p. 359. (Cited on pp. 599, 606, 607)

[69] R. Shapiro, *The use of linear filtering as a parameterization of atmospheric diffusion*, J. Atmos. Sci., 28 (1971), pp. 523–531. (Cited on p. 606)

[70] R. Shapiro, *Linear filtering*, Math. Comp., 29 (1975), pp. 1094–1094. (Cited on p. 606)

[71] C.-W. Shu and S. Osher, *Efficient implementation of essentially non-oscillatory shock-capturing schemes*, J. Comput. Phys., 77 (1988), pp. 439–471. (Cited on p. 598)

[72] B. Sjögreen, *High order centered difference methods for the compressible Navier-Stokes equations*, J. Comput. Phys., 117 (1995), pp. 67–78. (Cited on p. 606)

[73] S. Smith, *Dynamical systems that perform the singular value decomposition*, Systems Control Lett., 16 (1991), pp. 319–327. (Cited on p. 598)

[74] D. Subramani and P. F. J. Lermusiaux, *Energy-optimal path planning by stochastic dynamically orthogonal level-set optimization*, Ocean Modeling, 100 (2016), pp. 57–77. (Cited on pp. 598, 601)

[75] D. Tang, F. W. Schwartz, and L. Smith, *Stochastic modeling of mass transport in a random velocity field*, Water Resources Res., 18 (1982), pp. 231–244. (Cited on p. 597)

[76] L. N. Trefethen and D. Bau III, *Numerical Linear Algebra*, SIAM, 1997. (Cited on p. 613)

[77] J. Tryoen, O. L. Maître, M. Ndjinga, and A. Ern, *Intrusive Galerkin methods with upwinding for uncertain nonlinear hyperbolic systems*, J. Comput. Phys., 229 (2010), pp. 6485–6511. (Cited on pp. 598, 605)

[78] J. H. Tu, C. W. Rowley, D. M. Luchtenburg, S. L. Brunton, and J. N. Kutz, *On dynamic mode decomposition: Theory and applications*, J. Comput. Dynam., 1 (2014), pp. 391–421. (Cited on p. 598)

[79] M. P. Ueckermann, P. F. J. Lermusiaux, and T. P. Sapsis, *Numerical Schemes and Studies for Dynamically Orthogonal Equations of Stochastic Fluid and Ocean Flows*, MSEAS Report 11, Department of Mechanical Engineering, MIT, Cambridge, MA, 2011. (Cited on pp. 610, 613)

[80] M. P. Ueckermann, P. F. J. Lermusiaux, and T. P. Sapsis, *Numerical schemes for dynamically orthogonal equations of stochastic fluid and ocean flows*, J. Comput. Phys., 233 (2013), pp. 272–294. (Cited on pp. 598, 601, 602, 605, 608, 610, 611, 612, 613, 618)

[81] X. Wan, D. Xiu, and G. E. Karniadakis, *Stochastic solutions for the two-dimensional advection-diffusion equation*, SIAM J. Sci. Comput., 26 (2004), pp. 578–590, https://doi.org/10.1137/S106482750342684X. (Cited on p. 598)

[82] M. O. Williams, I. G. Kevrekidis, and C. W. Rowley, *A data–driven approximation of the Koopman operator: Extending dynamic mode decomposition*, J. Nonlinear Sci., 25 (2015), pp. 1307–1346. (Cited on p. 598)

[83] P. D. Williams, *Achieving seventh-order amplitude accuracy in leapfrog integrations*, Monthly Weather Rev., 141 (2013), pp. 3037–3051. (Cited on p. 606)

[84] D. Xiu and G. E. Karniadakis, *Modeling uncertainty in flow simulations via generalized polynomial chaos*, J. Comput. Phys., 187 (2003), pp. 137–167. (Cited on p. 598)